Phase Separation and Nematic Order in Lyotropic Solutions: Two Types of Polymers with Different Stiffness in a Common Solvent

Sergei A. Egorov,[*,†,§] Andrey Milchev,[‡,§] Arash Nikoubashman,[¶] and Kurt Binder[*,¶]

†*Department of Chemistry, University of Virginia, Charlottesville, Virginia 22901, USA*

‡*Institute of Physical Chemistry, Bulgarian Academy of Sciences, 1113 Sofia, Bulgaria*

¶*Institute of Physics, Johannes Gutenberg University Mainz, Staudingerweg 7, 55128 Mainz, Germany*

§*Institute of Physics, Johannes Gutenberg University Mainz, Staudingerweg 7, 55128 Mainz, Germany*

E-mail: sae6z@cms.mail.virginia.edu; kurt.binder@uni-mainz.de

Abstract

The interplay of the isotropic-nematic transition and phase separation in lyotropic solutions of two types of semiflexible macromolecules with pronounced difference in chain stiffness is studied by Density Functional Theory and Molecular Dynamics simulations. While the width of the isotropic-nematic two-phase coexistence region is narrow for solutions with a single type of semiflexible chain, the two-phase coexistence region widens for solutions containing two types of chains with rather disparate stiffness. In the nematic phase, both types of chains contribute to the nematic order, with intermediate values of the order parameter compared to the corresponding single component solutions. As the difference in bending stiffness is increased, the two chain types separate into two coexisting nematic phases. The phase behavior is rationalized by considering the chemical potentials of the two components and the Gibbs excess free energy. The geometric properties of the chain conformations under the various conditions are also discussed.

1 Introduction

Blending two different types of polymers may yield materials with some properties superior to those of their constituents.[1–5] However, discussions in the literature focused almost exclusively on the behavior of mixtures of two flexible polymers. In fact, typical theoretical treatments of polymer miscibility along the lines of the standard Flory-Huggins theory[1–7] do not consider at all whether or not there is an effect of polymer chain stiffness on the mixing behavior. Semiflexible polymers are an interesting class of materials for various applications due to their liquid crystalline phases,[8–10] such as fibers with high tensile strength,[8] *etc.* Solutions containing different kinds of semiflexible biopolymers, *e.g.*, actin filaments and microtubules, play also an important role in various biophysical/biochemical contexts.[11–13] While suspensions of different kinds of viruses, which can be considered as almost completely rigid rods, have been studied both experimentally[14] and theoretically,[15,16] (binary) mixtures

of less stiff semiflexible macromolecules in a good solvent have been only rarely considered.[17]

The processing of polymer blends often begins with the preparation in a common solvent. If a semiflexible polymer in solution exhibits a transition from the isotropic phase to the nematic phase, then the location of this transition depends distinctly on chain stiffness.[8–10,18–20] In lyotropic solutions, where all monomer-monomer interactions are purely repulsive, the transition is solely driven by entropic effects.[18–26] Thus, even in a good solvent a nontrivial and interesting phase behavior arises for solutions containing two different semiflexible polymers. While the phenomenological Flory-Huggins theory of polymer miscibility was extended to ternary systems (polymer A–polymer B–solvent) in early work[27] and corresponding measurements on such systems were reported as early as 1947 for 35 pairs of polymers in various solvents common to both polymers,[28] mostly more or less flexible polymers were considered. Somewhat more recent work on the phase behavior of liquid crystalline polymer blends in a common solvent was reviewed by Dutta *et al.*[29], but a systematic study of the properties of such systems is not yet available. So far, theoretical work has mostly focused on thermotropic systems, where phase separation is driven by temperature, or on the extreme case of suspensions of flexible polymer coils plus hard rods[30–35] or binary mixtures of hard rods.[34,36]

In this work, we focus on the case of two semiflexible polymers where one constituent has a persistence length (ℓ_p) comparable to the contour length (L) of the chain, while the other constituent has a distinctly larger but finite persistence length. Thus, the considered situation is complementary to the case of solutions where both polymers have contour lengths much larger than their persistence lengths, as studied in the pioneering work of Semenov and Subbotin.[17] We occasionally include the case of fully rigid rods in our comparative study too, in order to emphasize the point that chains with large but finite $\ell_\mathrm{p}/L \gg 1$ still differ significantly from the limit of fully rigid rods ($\ell_\mathrm{p}/L \to \infty$). We present computations for generic coarse-grained models, such as tangent hard sphere chains or bead-spring models, both complemented by a suitable bond-angle potential to include the chain stiffness. We

assume the same perfect solvent quality for both polymers, so apart from the disparity of persistence length there are no interactions that distinguish them. We study these models by Density Functional Theory (DFT)[26,37] and Molecular Dynamics (MD) simulations, obtaining typical phase diagrams with mole fraction of the stiffer polymer and total monomer concentration as control variables. We pay particular attention to the properties of the possible nematic order and its effect on the chain conformations in these systems. In this way, we elucidate the interplay of mixing behavior and nematic order.

In most real solutions containing two types of semiflexible polymers, however, one will encounter a much more complicated situation: electrostatic interactions due to ions in the solution and (partial) charges on the effective monomeric units, disparity in size and shape of these units, different Flory-Huggins parameters for both polymers *etc.* may exist in addition to the difference in persistence lengths. Therefore, isotropic-isotropic (I-I) phase separation competes with the isotropic-nematic (I-N) phase separation in some systems.[29] While our model calculations are somewhat too restrictive to describe real experimental data, we consider it as a key advantage of our coarse-grained model that the effects of these various contributions can be separately studied. Hence, we can isolate their influence on the observed phase behavior and relevant physical properties, which helps to improve our understanding of these complex materials.

2 Models and Computational Methods

We consider two types of polymers A and B, which have equal contour lengths L_{A} and L_{B} as well as identical sizes of their effective monomeric units. The only asymmetry of these two constituents is a mismatch between their persistence lengths, $\ell_{\mathrm{p}}^{\mathrm{A}} < \ell_{\mathrm{p}}^{\mathrm{B}}$. Solvent particles are not explicitly included, but instead their effect is included implicitly in the effective (pairwise) interaction between the monomeric units (details provided below). Considering lyotropic solutions only, these interactions are purely repulsive and identical for the A-A,

A-B, and B-B pairs. According to the quasi-atomistic interpretation of the Flory-Huggins χ interaction parameter in solution, χ would be proportional to the difference in repulsion energies[1–6]

$$\varepsilon_{\mathrm{AB}} - (\varepsilon_{\mathrm{AA}} + \varepsilon_{\mathrm{BB}})/2 = 0 \tag{1}$$

since $\varepsilon_{\mathrm{AA}} = \varepsilon_{\mathrm{AB}} = \varepsilon_{\mathrm{BB}}$ for this choice of excluded volume interaction. Following this reasoning, no unmixing would be expected.

Alternatively, a quasi-macroscopic interpretation of χ can be adapted in terms of an effective contribution to the total free energy of mixing, where χ is defined by[1–6]

$$\frac{\Delta F_{\mathrm{mix}}}{k_{\mathrm{B}}T} = \frac{\phi_{\mathrm{A}}}{N_{\mathrm{A}}} \ln \phi_{\mathrm{A}} + \frac{\phi_{\mathrm{B}}}{N_{\mathrm{B}}} \ln \phi_{\mathrm{B}} + \chi \phi_{\mathrm{A}} \phi_{\mathrm{B}}, \tag{2}$$

where ϕ_{A} and ϕ_{B} are volume fractions taken by the effective monomeric units on some underlying lattice. In this picture, the physical origin of the deviation of the free energy of mixing from the expression for an ideal mixture is not specified, and hence χ can become nonzero due to nontrivial entropic effects when a stiffness disparity is present.[38–40] We shall analyze to what extent such effects matter for our model.

In our DFT calculations, we model the polymer chains as a sequence of $N_{\mathrm{A}} = N_{\mathrm{B}} = N$ tangent hard spheres of diameter $\sigma_{\mathrm{A}} = \sigma_{\mathrm{B}} = \sigma$, so that the contour length is $L = (N-1)\sigma$ for both species.[26] Bending stiffness is included through the potential

$$U_{\mathrm{bend}}(\theta_{ijk}) = \varepsilon_{\mathrm{bend}}[1 - \cos(\theta_{ijk})] \tag{3}$$

where θ_{ijk} is the bond angle formed by the two bond vectors $\mathbf{a}_i = \mathbf{r}_j - \mathbf{r}_i$ and $\mathbf{a}_j = \mathbf{r}_k - \mathbf{r}_j$ between the three subsequent monomeric units i, j, and k. The interaction strength is set by the parameter $\varepsilon_{\mathrm{bend}}$, which controls the persistence length ℓ_{p}. The latter is normally introduced as[5]

$$\langle \mathbf{a}_i \cdot \mathbf{a}_{i+s} \rangle \propto \exp\left(-s\ell_{\mathrm{b}}/\ell_{\mathrm{p}}\right) \tag{4}$$

for $s = 1, 2, 3, \ldots$, and $s\ell_\mathrm{b} \ll \ell_\mathrm{p}$, with (average) bond length ℓ_b. For $\kappa \equiv \varepsilon_\mathrm{bend}/(k_\mathrm{B}T) \gtrsim 2$ and polymer concentrations in the isotropic regime, one finds

$$\ell_\mathrm{p} \approx \ell_\mathrm{b}\kappa \, . \tag{5}$$

For the MD simulations, we describe the excluded volume interactions through the purely repulsive Weeks-Chandler-Andersen (WCA) potential[41]

$$U_\mathrm{WCA}(r) = \begin{cases} 4\varepsilon \left[\left(\frac{\sigma}{r}\right)^{12} - \left(\frac{\sigma}{r}\right)^{6} \right] + \varepsilon, & r \leq 2^{1/6}\sigma \\ 0, & r > 2^{1/6}\sigma \end{cases} , \tag{6}$$

where $\varepsilon \equiv k_\mathrm{B}T$ controls the strength of the interaction.

Bonds between neighboring monomeric units are realized through the finitely extensible nonlinear elastic (FENE) potential[42]

$$U_\mathrm{FENE}(r) = \begin{cases} -\frac{kr_0^2}{2} \ln \left[1 - \left(\frac{r}{r_0}\right)^2 \right], & r < r_0 \\ \infty, & r \geq r_0. \end{cases} \tag{7}$$

The spring constant is chosen as $k = 30\,\varepsilon/\sigma^2$ and the maximum bond length is set to $r_0 = 1.5\,\sigma$, resulting in an average bond length of $\ell_\mathrm{b} \approx 0.97\,\sigma$ for both polymer types. The contour lengths of the polymers are then $L = (N-1)\ell_\mathrm{b} \approx (N-1)\sigma$, which are close to those of the tangent hard sphere chain.

Bending stiffness is included using the same potential U_bend as in in our DFT model [see Eq. (3)]. The difference in bending stiffness $\kappa_\mathrm{A} < \kappa_\mathrm{B}$ is the only parameter distinguishing the two polymer types. As a result, the conformations of A chains and B chains at given osmotic pressure P (or volume fraction ϕ of effective monomeric units) differ, due to the difference in stiffnesses $\kappa_\mathrm{A} < \kappa_\mathrm{B}$ [or persistence lengths, *cf.* Eq. (5), respectively]. In the occurring nematic phases, the nematic order parameters S_A and S_B of A and B chains also

differ. These differences are particularly significant if the stiffness disparity is large, and hence we focus on this case in the present paper. Further, unless stated otherwise explicitly, we consider semiflexible polymers consisting of $N_{\rm A} = N_{\rm B} = N = 16$ monomeric units.

In the MD simulations, the monomeric units are assigned a mass $m_{\rm A} = m_{\rm B} = m$, and a barostat[43,44] or standard Langevin thermostat[42] is applied to realize $\mathcal{N}PT$ or $\mathcal{N}VT$ ensembles, respectively ($\mathcal{N}$ being the total number of monomeric units). With our choice of units, the intrinsic MD time unit is $\tau_{MD} = \sqrt{m\sigma^2/\varepsilon}$, and the time step for the numerical integration of motion was $\Delta t = 0.005\,\tau_{\rm MD}$. Simulations were performed in rectangular boxes with periodic boundary conditions throughout. Starting configurations were generated by placing stretched out chains in the simulation box. Initially, all bond angles were zero and the chains were oriented along the z-direction. The number of chains was chosen according to the desired average density in the box and composition $X_{\rm B}$ corresponding to the chemical nature of the chains as A or B in this state. The systems contained typically $\mathcal{N} = 10^5$ to 10^6 particles, and simulations were performed for 10^8 to 10^9 integration steps to achieve proper equilibration and the necessary statistical accuracy. This runtime was long enough so that individual chains could diffuse throughout the box, irrespective of whether the system was in the isotropic or nematic phase. This large computational effort was possible due to the availability of graphics processing units (GPUs) employing the HOOMD-blue software.[45]

For homogeneous systems of one kind of semiflexible chains, DFT is based on the minimization of a free energy functional F using the orientational distribution function $f(\omega)$ of the bond vectors (ω stands for their two polar angles). This free energy functional contains an ideal part and an excess part. The latter (when normalized per molecule) can be written as

$$F_{\rm exc}N/(\mathcal{N}k_{\rm B}T) = \frac{\rho_{\rm mol}}{2}\int {\rm d}\omega \int {\rm d}\omega' f(\omega)f(\omega')V_{\rm excl}(\omega,\omega') \quad , \tag{8}$$

where $\rho_{\rm mol} = \rho/N$ is the molecular concentration, and $V_{\rm excl}(\omega,\omega')$ is the excluded volume between the monomers of two chains with orientations ω and ω', respectively. While $V_{\rm excl}(\omega,\omega')$ can be obtained analytically in the limiting case of rigid rods[46], it can only be obtained ap-

proximately for semiflexible polymers (*e.g.* Ref. 18–26).

While a treatment in terms of the second virial approximation suffices for suspensions of long thin hard rods, Eq. (8), the extension to solutions of semiflexible polymers is highly nontrivial for several reasons: (i) for long thin hard rods the onset of nematic order occurs already at small ρ_{mol} so that effects due to higher order virial coefficients are negligible. For semiflexible polymers, however, this transition to nematic order shifts to higher concentration with decreasing chain stiffness, and therefore the second virial approximation no longer suffices. (ii) The orientation of a hard rod is fully characterized by the two polar angles symbolically denoted by ω, but a separate degree of freedom is needed to describe the orientation of each bond vector of the chain molecule (or the tangent vector along the contour $\mathbf{r}(s)$ if one uses the Kratky-Porod continuum approximation of the polymer in terms of a space curve $\mathbf{r}$ with coordinate s along this curve).

There are different ways to deal with this issue: Khokhlov and Semenov[21,22] and later Odijk[23] and Chen[24] based their treatment on the Kratky-Porod model in an effective field provided by the other chains, still relying on the second virial approximation. It is believed that this theory (which requires extensive numerical work[24]) is accurate when $\ell_{\mathrm{p}}/\ell_{\mathrm{b}} \gg 1$, and then ℓ_{p}/L is a single nontrivial parameter of the theory. However, an accurate extension to chains of intermediate stiffness $\ell_{\mathrm{p}}/\ell_{\mathrm{b}} \sim \mathcal{O}(10)$, where effects due to higher order virial terms would matter, is not known. In this work, we adapt the alternative approach proposed by Fynewever and Yethiraj,[47] where the semiflexible chains are coarse-grained to effective rod-like objects. In that model, $V_{\mathrm{excl}}(\omega, \omega')$ in Eq. (8) describes the excluded volume between two chains. Then, the angles ω and ω' describe the average orientation of the entire chains, characterized by the vector belonging to the smallest eigenvalue of the moment of inertia tensor. One can simplify the description further noting that V_{excl} does not depend on the two chain orientations separately, but only on their relative angle ϑ. For very thin hard rods

of length $L/\sigma \gg 1$ (with rod diameter σ), $V_{\rm excl}(\vartheta)$ has a simple analytic form:

$$V_{\rm excl}(\vartheta) = 2\sigma L^2 \sin(\vartheta). \tag{9}$$

When the thickness of the rod is non-negligible, one finds[46]

$$V_{\rm excl}(\vartheta) = \left[2\sigma L^2 + (\pi/2)\sigma^3\right] \sin(\vartheta) + \left[(\pi/2)(1+|\cos(\vartheta)|) + 2E(\sin(\vartheta))\right] \sigma^2 L, \tag{10}$$

with $E(\sin(\vartheta)) = \int_0^{\pi/2} \left[1 - \sin(\vartheta)^2 \sin(\varphi)^2\right]^{1/2} {\rm d}\varphi$ being the complete elliptic integral of the second kind.

For semiflexible chains, $V_{\rm excl}$ is a nontrivial quantity which needs to be computed numerically, *e.g.*, by Monte Carlo (MC) calculations.[47] In practice, $V_{\rm excl}$ is determined for seven relative orientations $0 \leq \theta \leq \pi/2$, and then fitted to a function to interpolate between these points[47]

$$V_{\rm excl}(\gamma) = c_1 + c_2 \left[1 - c_3 \cos(\vartheta)^2\right]^{1/2} \tag{11}$$

with fitting constants c_1, c_2, and c_3. The resulting excluded volume is also proportional to L^2, as for the case of two rigid rods [*cf.* Eq. (10)], but there are several distinct differences which will be discussed below.

Figure 1(a) shows how $V_{\rm excl}(\vartheta)$ changes with varying persistence length. For ϑ near $\pi/2$, the data for large $\ell_{\rm p}$ are close to the rigid rod limit. However, the intercept at $\vartheta = 0$ is much larger for a pair of semiflexible polymers compared to a pair of rigid rods, and the increase of $V_{\rm excl}$ near $\vartheta = 0$ is quadratic in ϑ rather than linear. This difference can be understood when one considers that the individual bond vectors are not strictly parallel to the average orientation of the whole chain, so the choice $\vartheta = 0$ is not qualitatively distinct from small non-zero values of ϑ. Further, the transverse linear dimension $\ell_{\rm t}$ of semiflexible chains (see Ref. 48 and references therein) is distinctly larger than unity. We speculate that these factors enter the prefactor of the correction term for $\vartheta = 0$. Similarly, the leading term no longer has

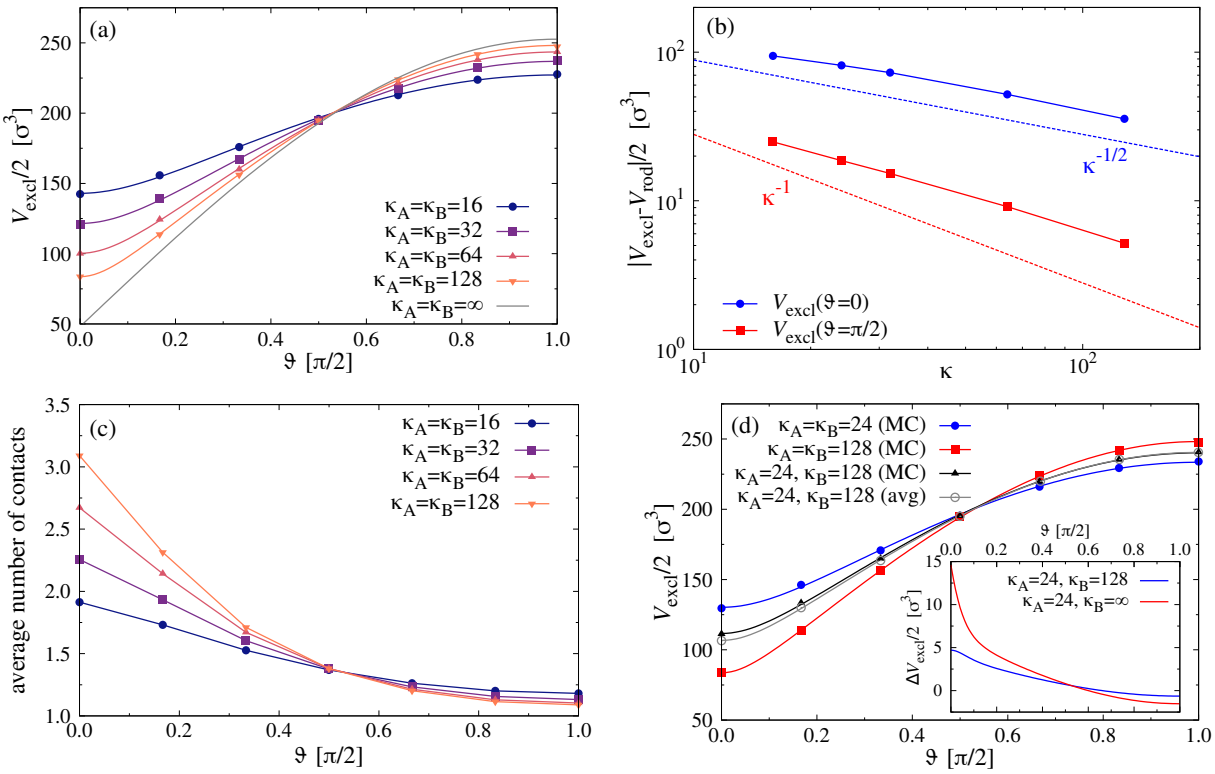

Figure 1: (a) Excluded volume for five different values of $\kappa_A = \kappa_B$, as indicated. (b) Difference in V_{excl} between a pair of semiflexible chains with $\kappa_A = \kappa_B$ and a pair of stiff rods at angles $\vartheta = 0$ and $\vartheta = \pi/2$. The blue dashed line shows $\kappa^{-1/2}$ while the red dashed line shows κ^{-1}. (c) Average number of chain contacts for the semiflexible cases as shown in (a). (d) Excluded volume for $\kappa_A = 24$ and $\kappa_B = 128$ and compared to the average (see text). The inset shows the difference in excluded volume, $\Delta V/2 = [V_{excl}^{AB}(\vartheta) - V_{excl}^{avg}(\vartheta)]/2$, for the two cases $\kappa_A = 24$, $\kappa_B = 128$ and $\kappa_A = 24$, $\kappa_B = \infty$.

a prefactor $2\sigma L^2 + (\pi/2)\sigma^3$ [*cf.* Eq. (10)], but is reduced due to chain bending. For instance, the mean squared end-to-end distance in the above-mentioned examples is $\langle R_e^2 \rangle = 204\,\sigma^2$ ($\kappa = 128$) and $\langle R_e^2 \rangle = 173\,\sigma^2$ ($\kappa = 16$) rather than $L^2 = \ell_b^2 (N-1)^2 = 212\,\sigma^2$.

A closer examination of $V_{excl}(\vartheta = 0)$ and $V_{excl}(\vartheta = \pi/2)$ [Fig. 1(b)] shows that for $\vartheta = \pi/2$ the data converge to the rod limit from below with a variation proportional to $1/\ell_p$. This behavior is plausible, since the mean squared end-to-end distance of a flexible rod is reduced from the rigid rod limit by a correction of order $1/\ell_p$ according to the Kratky-Porod model. In contrast, for $\vartheta = 0$ the convergence to the limiting rod-like behavior is much slower, and follows a $1/\sqrt{\ell_p}$ law. This behavior can be understood if we recall that only for a pair of rigid rods $\vartheta = 0$ means that the rods are strictly parallel, while for a pair of semiflexible

polymers bond vector orientations deviate from the orientation of the whole chain by an amount of order $\sqrt{L/\ell_{\rm p}}$, for $\ell_{\rm p}/L \gg 1$ according to the Kratky-Porod model. Finally, we also draw attention to the fact that not only a single pair of monomer-monomer contacts contributes to the second virial coefficients between chains, but also a fraction of cases occur where several contacts contribute [Fig. 1(c)].

In our previous work,[26,49,50] we have used numerical MC results for $V_{\rm excl}(\vartheta)$ between two isolated chains[47] which then were appropriately rescaled.[26] In that case, DFT can be straightforwardly implemented to minimize the free energy functional and hence locate the I-N transition. However, the nematic order parameter S derived in this way refers to the chain ordering as a whole, and not to the order parameter $S_{\rm b}$ associated with individual bond vectors. As discussed by Tortora and Doye,[51] S typically exceeds $S_{\rm b}$ distinctly. It also has been suggested that the excluded volume interactions shown in Fig. 1 (calculated from two unconstrained chains in a large volume) is only accurate in the isotropic phase, since the stretching of the chains in the nematic phase along the director is not accounted for.[49]

While in our binary systems the excluded volume interactions between two monomeric units does not depend on the type of pair {AA, AB, and BB}, this is, however, no longer true when we consider $V_{\rm excl}$ between two coarse-grained chains. In this case, we must distinguish between $V_{\rm excl}^{\rm AA}(\vartheta)$, $V_{\rm excl}^{\rm AB}(\vartheta)$, and $V_{\rm excl}^{\rm BB}(\vartheta)$, which contain the information on the different chain stiffnesses $\kappa_{\rm A}$ and $\kappa_{\rm B}$. In Fig. 1(d), we compare the actual excluded volume interaction $V_{\rm excl}^{\rm AB}(\vartheta)$ between a pair of chains with $\kappa_{\rm A} = 24 < \kappa_{\rm B} = 128$ with the average $V_{\rm excl}^{\rm avg}(\vartheta) = \left[V_{\rm excl}^{\rm AA}(\vartheta) + V_{\rm excl}^{\rm BB}(\vartheta)\right]/2$. This comparison demonstrates that indeed an entropically driven Flory-Huggins parameter $\chi \propto V_{\rm excl}^{\rm AB} - V_{\rm excl}^{\rm avg}$ arises, although no such term exists in the monomer-monomer interaction. Despite the smallness of this effect, this entropy-driven Flory-Huggins parameter can have a pronounced effect on the phase behavior at high polymer concentrations, even leading to coexistence between two distinct nematic phases (one A-rich and the other B-rich), as is analyzed elsewhere in more detail.[40] Here, we shall focus on the effect of stiffness disparity on the isotropic-nematic phase separation in the mixed

systems.

3 Numerical Results

3.1 Phase diagrams for moderate stiffness mismatch

We start with a brief discussion of pertinent results of earlier related work. Phase equilibria in solutions of chains in the limit where the contour lengths of both types of chains are much larger than their persistence lengths have already been studied by Semenov and Subbotin,[17] by extending the Khokhlov-Semenov-Odijk approach.[21–24] Since this region of extremely long polymer chains is out of consideration here, we do not discuss the details of that work. Phase equilibria in binary mixtures of completely rigid and flexible molecules have been actively studied theoretically, both *via* various mean-field approaches[15,16,30,31,52–55] and by computer simulations.[33,56,57] Escobedo and de Pablo[33] studied a binary mixture of semiflexible and fully rigid 16-mers *via* MC simulations in the expanded Gibbs ensemble at constant pressure $P = 0.14\, k_{\mathrm{B}}T/\sigma^3$, which corresponds to the pressure reduced with respect to the I-N coexistence pressure of the rigid component equal to $P/P_{\mathrm{B}}^{\mathrm{coex}} = 1.3$. They have constructed the corresponding isobaric phase diagram in the plane of the inverse stiffness parameter of the semiflexible component A, κ_{A}^{-1}, *vs.* the mole fraction of the rigid component B, X_{B}. Their results are reproduced in Fig. 2, demonstrating that the two-phase region widens considerably with decreasing stiffness parameter κ_{A}.

In order to assess the accuracy of our DFT approach (see Sec. 2 for details), we determined the isobaric phase diagram for selected systems at the same pressure, $P/P_{\mathrm{B}}^{\mathrm{coex}} = 1.3$ ($P = 0.14\, k_{\mathrm{B}}T/\sigma^3$), as in the MC simulations of Escobedo and de Pablo[33]. To this end, we computed the four unknown quantities, *i.e.*, the mole fractions of the fully rigid component in the isotropic and nematic phases, $X_{\mathrm{B}}^{\mathrm{iso}}$ and $X_{\mathrm{B}}^{\mathrm{nem}}$, and the monomer number densities of the isotropic and nematic phases, ρ_{iso} and ρ_{nem}, from the four coexistence conditions, *i.e.*, $P_{\mathrm{iso}} = P_{\mathrm{nem}} = 0.14\, k_{\mathrm{B}}T/\sigma^3$, $\mu_{\mathrm{A}}^{\mathrm{iso}} = \mu_{\mathrm{A}}^{\mathrm{nem}}$, and $\mu_{\mathrm{B}}^{\mathrm{iso}} = \mu_{\mathrm{B}}^{\mathrm{nem}}$, where μ_i is the chemical potential

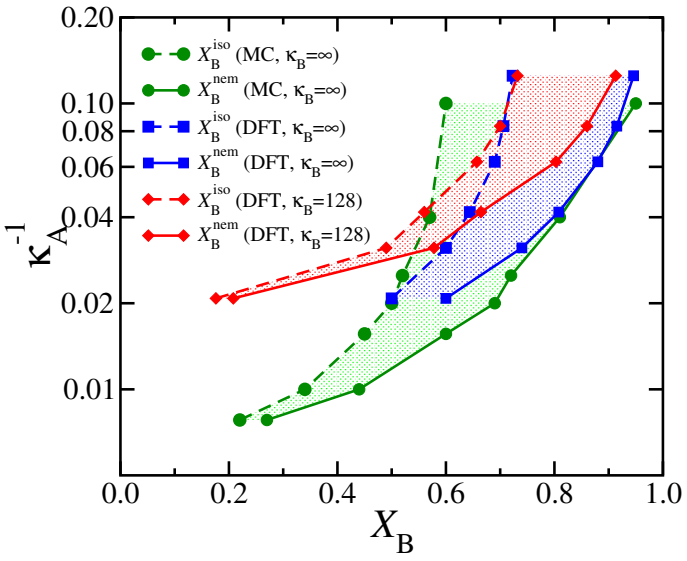

Figure 2: Phase diagram for a binary mixture of semiflexible and fully rigid 16-mers at constant pressure $P/P_{\rm B}^{\rm coex} = 1.3$ ($P = 0.14\,k_{\rm B}T/\sigma^3$) in the variables $\kappa_{\rm A}^{-1}$ and $X_{\rm B}$. MC simulation results by Escobedo and de Pablo[33] are shown as circles and our DFT results are plotted as squares (lines are drawn to guide the eye). Also shown (as diamonds) are the DFT results for a binary mixture of semiflexible 16-mers with fixed $\kappa_{\rm B} = 128$ and variable $\kappa_{\rm A}$, again at $P/P_{\rm B}^{\rm coex} = 1.3$ ($P = 0.18\,k_{\rm B}T/\sigma^3$).

of the $i^{\rm th}$ component. The corresponding DFT results are also shown in Fig. 2, and the overall agreement with the previous MC simulations is reasonable, albeit DFT consistently underestimates the width of the biphasic region. In addition, we show DFT results for binary mixtures where the second component is not a fully rigid rod, but rather semiflexible with large stiffness parameter $\kappa_{\rm B} = 128$, again at $P/P_{\rm B}^{\rm coex} = 1.3$ ($P = 0.18\,k_{\rm B}T/\sigma^3$). One sees a pronounced difference from the rigid case, and we will return to this point below.

To illustrate in more detail how the DFT data in Fig. 2 were obtained, we plot in Fig. 3(a) the DFT phase diagram in the variables P *vs.* $X_{\rm B}$ for the cases $\kappa_{\rm A} = 32$ mixed with $\kappa_{\rm B} = 128$ (red lines) or $\kappa_{\rm B} = \infty$ (blue lines). The closed loops correspond to the I-N phase equilibrium, and one clearly sees that the two-phase region widens considerably and moves to larger values of $X_{\rm B}$ in going from $\kappa_{\rm B} = 128$ to $\kappa_{\rm B} = \infty$. Figure 3(b) shows the corresponding MD results for $\kappa_{\rm B} = 128$ which are similar to the DFT results, apart from the fact that MD predicts generally larger pressures for the I-N transition. For the mixtures with $\kappa_{\rm A} = 32$, no N-N coexistence has been found, at least for physically reasonable values of pressure. Given that

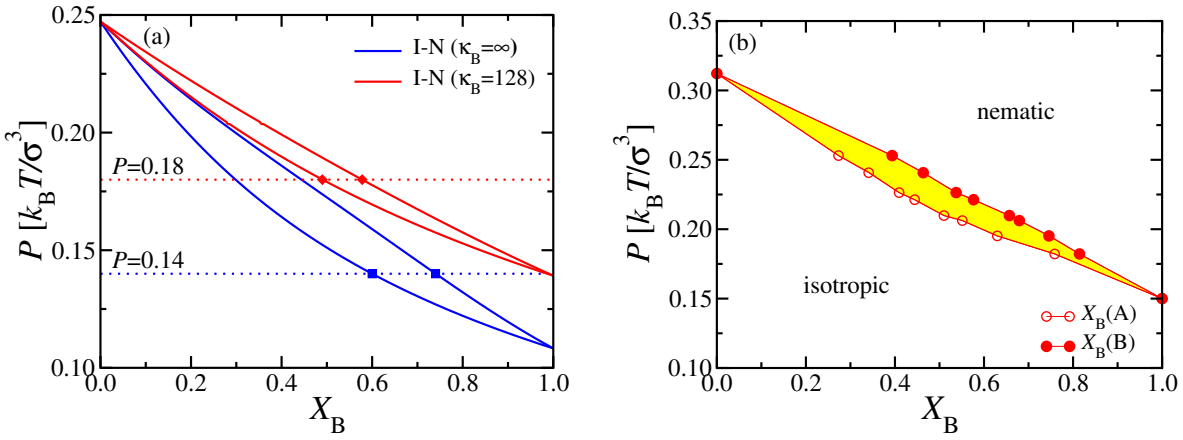

Figure 3: (a) Phase diagram from DFT for a binary mixture in the variables P *vs.* X_B for $\kappa_A = 32$, and two values of κ_B, as indicated. The closed loops indicate I-N coexistence, and the symbols indicate X_B in I and N phases at coexistence for $\kappa_B = \infty$ and $\kappa_B = 128$. (b) The same as in (a), but from MD simulations with $\kappa_A = 32$ and $\kappa_B = 128$. The mole fractions $X_B(A)$, $X_B(B)$ of the A- and B-rich domains at coexistence pressure are shown by open and filled symbols, respectively. The total number of beads in the simulated system is $\mathcal{N} = 406,272$.

such N-N coexistence is more likely for a larger stiffness disparity, we next consider the case $\kappa_A = 24$, keeping the same two values of κ_B as before. The corresponding DFT phase diagrams are shown in Fig. 4(a), which reveal N-N phase coexistence for the case of the fully rigid second component ($\kappa_B = \infty$), but not for the case of the semiflexible one ($\kappa_B = 128$), at least for physically reasonable values of pressure.

In Fig. 4(b), we show the MD counterpart of the DFT results for $\kappa_A = 24$, $\kappa_B = 128$ in the P-X_B plane. The qualitative behavior of the DFT phase diagram is well reproduced, though there are systematic differences in quantitative respects. DFT predicts distinctly lower pressures for the I-N two-phase coexistence region, as well as for the location of the I-N transition in the pure systems. We argue that these differences are not due to the (minor) differences of the models for the monomeric units (hard spheres in DFT *vs.* WCA beads in MD), but rather reflect systematic errors originating from the approximations involved in DFT, as discussed in Sec. 2. Apart from statistical errors [which are comparable to the size of the symbols in Fig. 4(b)], MD yields the numerically exact statistical mechanics of the model. However, the drawbacks of such computer simulations should not be forgotten:

Each state involving a pair of coexisting phases [shown by symbols in Fig. 4(b)] requires very extensive runs and cumbersome data analysis: so it is challenging to produce smooth curves for the phase boundaries [unlike Fig. 4(a)], and the data points are rather connected by straight lines, to guide the eye.

Figures 4(c) and 4(d) give some information on how the MD data for P-X_B phase diagrams are obtained. MD simulations of $\mathcal{N}/N = 25,392$ chains were conducted in an elongated box with periodic boundary conditions and an aspect ratio 3:1:1, keeping the fraction $X_\mathrm{B} = 0.5$ fixed. In thermal equilibrium, the pressure (which we compute from the virial theorem) is homogeneous in either phases. The situation is subtle if the chosen density ρ and composition X_B leads to a state that falls inside the coexistence region [see Fig. 4(b,c)]. Then two isotropic-nematic interfaces form [see Fig. 4(d)], which are aligned normal to the long direction and parallel to the director, biased by the initial condition. Figure 4(c) shows the monomeric density profiles in the box for the case where the total density of monomeric units is $\rho = 0.37\,\sigma^{-3}$, for both components ρ_A and ρ_B. From this plot one can also recognize that the total monomer density in the B-rich phase is higher than in the A-rich phase, with $\rho(\mathrm{A}) = 0.355\,\sigma^{-3}$ and $\rho(\mathrm{B}) = 0.385\,\sigma^{-3}$ in this example. Qualitatively this difference in monomer density between coexisting phases is compatible with the DFT predictions (Fig. 5). This behavior indicates that the "packing" of the nematically ordered chains is "easier" than in a dense isotropic phase, where both types of chains are randomly oriented.

Since the coexisting phases differ both in their composition and in their total density [see Fig. 4(c)], the systems need to be equilibrated carefully: The driving forces for the associated interdiffusion of chains are small, so that long simulation times are needed to reach equilibrium. For state points where the volume fraction of the minority phase is small, it occurs that phase separation is not seen because the lifetime of metastable mixed (isotropic or nematic) states is too large. Further, finite size effects might also matter if there is not enough space to form the two interfaces enclosing a small domain. This is a particular problem when the width ΔX_B of the I-N coexistence region is small, which impeded the

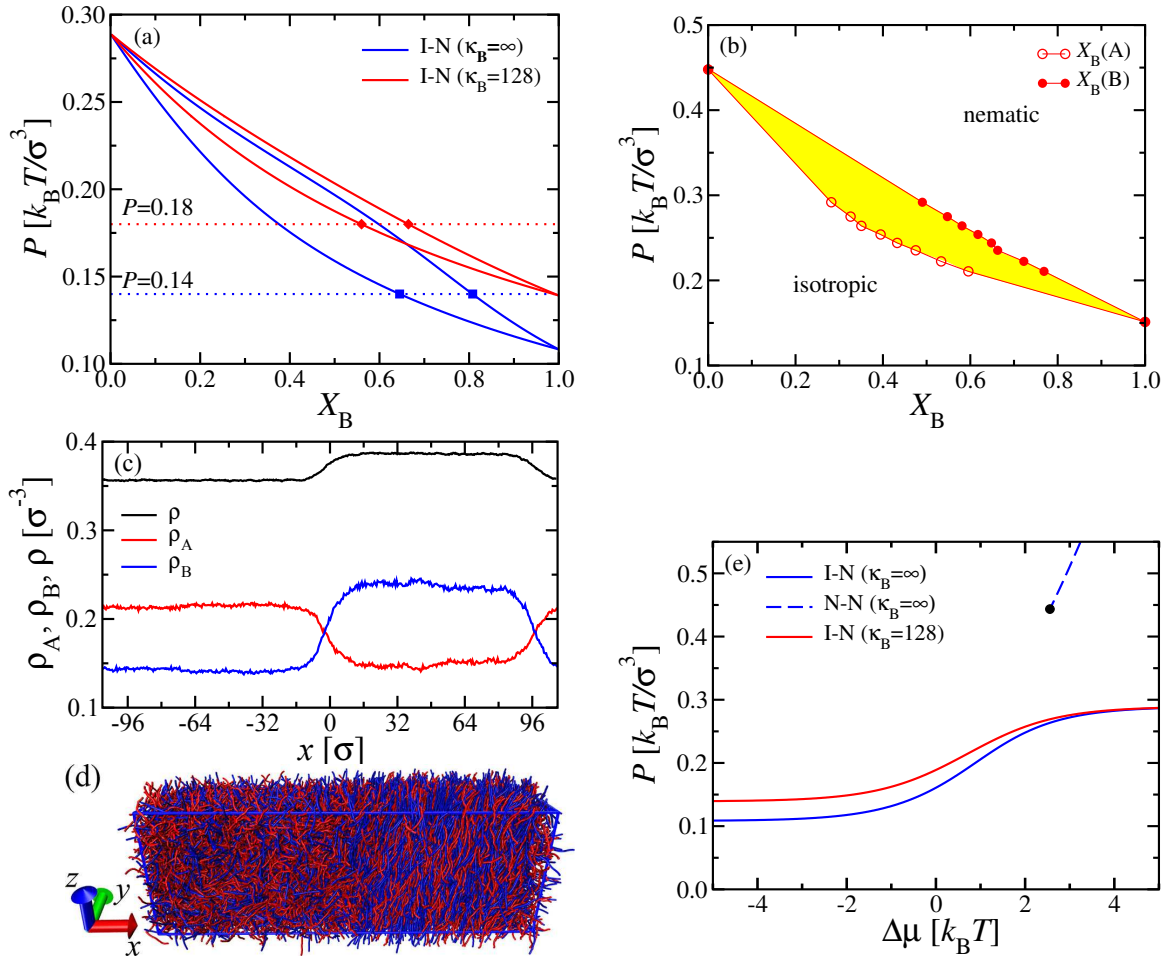

Figure 4: (a) Phase diagram from DFT in the variables P *vs.* X_B for $\kappa_\mathrm{A} = 24$, and two values of κ_B, as indicated. The closed loops indicate I-N coexistence, and the symbols show X_B in I and N phases at coexistence at $P = 0.14\,k_\mathrm{B}T/\sigma^3$ ($P = 0.18\,k_\mathrm{B}T/\sigma^3$) for $\kappa_\mathrm{B} = \infty$ ($\kappa_\mathrm{B} = 128$), *i.e.*, $P/P_\mathrm{B}^\mathrm{coex} = 1.3$ in both cases. (b) The same as in (a), but from MD simulations with $\kappa_\mathrm{A} = 24$ and $\kappa_\mathrm{B} = 128$. The mole fractions X_B(A), X_B(B) of the A- and B-rich domains at coexistence pressure are shown by open and filled symbols, respectively. (c) Density profiles of A-monomers (ρ_A, red) and of B-monomers (ρ_B, blue) as well as of the total monomer density ($\rho = \rho_\mathrm{A} + \rho_\mathrm{B}$, black) along the x-axis of the simulation box [see (d)] for total monomer density $\rho = 0.37\,\sigma^{-3}$ and composition $X_\mathrm{A} = X_\mathrm{B} = 0.5$. (d) A snapshot of the same system shown in (c). Polymers with stiffness $\kappa_\mathrm{A} = 24$ are shown in red, those with $\kappa_\mathrm{B} = 128$ in blue. (e) Same as (a) but in the variables P *vs.* $\Delta\mu = \mu_\mathrm{A} - \mu_\mathrm{B}$. The solid lines indicate I-N coexistence, while the dashed line shows N-N coexistence with the critical point marked by a circle. No N-N coexistence was found for $\kappa_\mathrm{B} = 128$.

recording of data points to characterize phase coexistence near the pure phases. Even when phase separation in the simulation box is observed, quantitative analysis of these states is difficult: The positions of the two interfaces are not known beforehand, and they diffuse over the course of the simulation. Hence, the interface positions need to be determined first, and then the densities of the two species in the pure phases can be computed away from the interfaces. Further, MD cannot yield a counterpart of the phase diagram in the space of only intensive thermodynamic variables [Fig. 4(e)]. Thus, MD simulations are rather inconvenient for gaining a quick overview for a broad range of parameters (N, κ_{A}, κ_{B}, P), and DFT is to be preferred. The MD simulations are crucial, however, to obtain some information on the numerical accuracy of the DFT calculations due to the approximations discussed in Sec. 2. The comparison between Fig. 4(a) and the (in principle more reliable) Fig. 4(b) suggests that the qualitative trends predicted by DFT are correct.

In Fig. 4(e) we re-plot the DFT phase diagrams for the same two binary mixtures in intensive variables, *i.e.*, pressure P *vs.* the difference of the chemical potentials of the two components $\Delta\mu = \mu_{\mathrm{A}} - \mu_{\mathrm{B}}$. Finally, in Fig. 5 we provide another representation of the phase diagrams for (a) $\kappa_{\mathrm{A}} = 24$ and $\kappa_{\mathrm{B}} = 128$ as well as (b) $\kappa_{\mathrm{A}} = 24$ and $\kappa_{\mathrm{B}} = \infty$, in the variables ρ *vs.* X_{B}. While the tie lines of the pure phases ($X_{\mathrm{B}} = 0$ and 1) are strictly parallel to the ordinate axis, for the mixed phases they form a nontrivial angle with the ordinate. This angle increases the more one moves away from the pure phases. Note that this effect is more pronounced for $\kappa_{\mathrm{B}} = \infty$, which can be seen as a precursor effect of a triple point between the isotropic phase and two different nematic phases, occurring for still smaller κ_{A} (see Sec. 3.5 below).

3.2 Thermodynamic Potentials

In this section, we rationalize the observed marked difference between the phase behavior of the two cases $\kappa_{\mathrm{B}} = 128$ and $\kappa_{\mathrm{B}} = \infty$, namely the absence of N-N phase coexistence in the former case (for physically accessible pressures) and its presence in the latter case. Under-

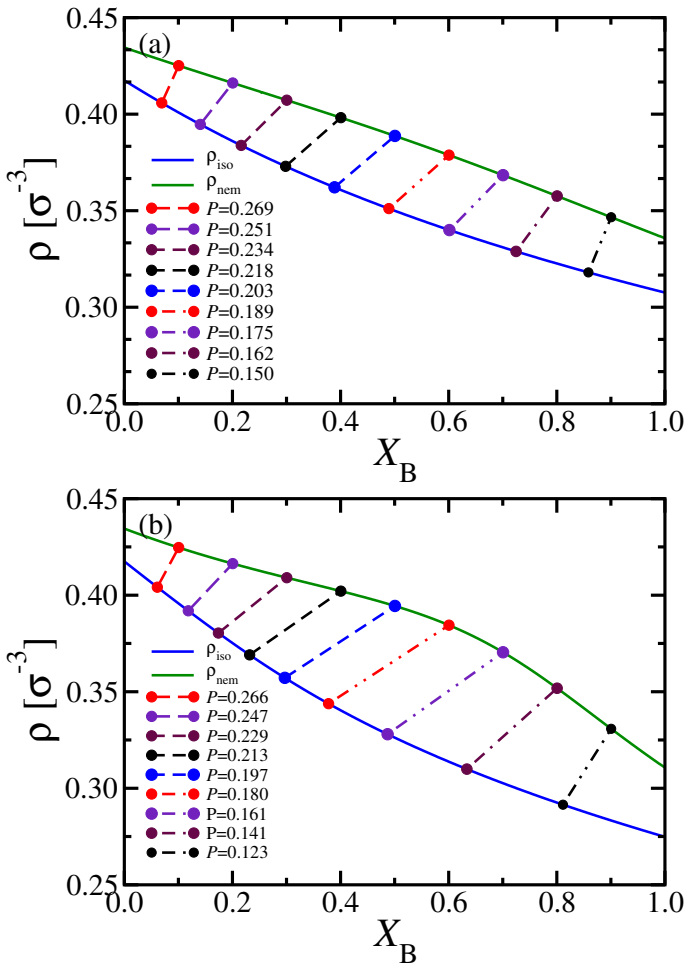

Figure 5: Phase diagram for a binary mixture with $\kappa_A = 24$ and (a) $\kappa_B = 128$ and (b) $\kappa_B = \infty$. Data are shown in the variables ρ *vs.* X_B. In both panels, solid lines correspond to I-N coexistence phase boundaries (blue – isotropic branch and green – nematic branch), while dashed lines with symbols indicate tie-lines connecting coexisting phases at 9 different values of the pressure P, as indicated in the legend.

standing the difference in phase behavior between solutions of very stiff macromolecules and strictly rigid rods may be of interest in many cases of physical significance, *e.g.*, suspensions of various viruses. To this end, we consider the chemical potentials of the two components and the Gibbs excess free energy $G_{\rm exc}$ (defined relative to the ideal binary mixture) as a function of X_B. These two quantities are plotted in Fig. 6(a,b) at a reduced pressure $P/P_B^{\rm coex} = 1.3$, *i.e.*, $P = 0.18\, k_B T/\sigma^3$ for $\kappa_B = 128$ and $P = 0.14\, k_B T/\sigma^3$ for $\kappa_B = \infty$, respectively, thereby corresponding to the region of I-N phase coexistence in the phase diagram. The symbols indicate the coexistence points, *i.e.*, Fig. 6(a) illustrates the standard "equal area" construc-

tion for the phase equilibrium, while Fig. 6(b) shows the "common tangent" construction. One observes that the curve for $G_{\rm exc}$ for the case $\kappa_{\rm B} = 128$ is always below the corresponding curve for the fully rigid case, $\kappa_{\rm B} = \infty$. However, as already shown in Fig. 5, the I-N phase separation is observed for both values of $\kappa_{\rm B}$, *i.e.*, the difference between the two cases is only quantitative, with a more narrow biphasic region for $\kappa_{\rm B} = 128$ compared to rigid rods, but not qualitative.

Note that the variation of $\Delta\mu - \Delta\mu_{\rm coex}$ seen in Fig. 6(a) is not similar to the van der Waals loop known from the vapor-liquid transition or the equivalent problem of unmixing for a binary fluid. In the latter case, we find a smooth loop with $\partial(\Delta\mu)/\partial X_{\rm B} < 0$ from $X_{\rm B,1}^{\rm coex}$ up to a spinodal point $X_{\rm B,1}^{\rm s}$, and from a second spinodal point $X_{\rm B,2}^{\rm s}$ to $X_{\rm B,2}^{\rm coex}$; these regimes are interpreted as metastable A-rich and B-rich states, while homogeneous states with $\partial(\Delta\mu)/\partial X_{\rm B} > 0$ between $X_{\rm B,1}^{\rm s}$ and $X_{\rm B,2}^{\rm s}$ would be unstable. In the present case, the behavior is completely different: The metastable branches of $G_{\rm exc}$ that represent homogeneous mixtures in the regime $X_{\rm B,1}^{\rm s} < X_{\rm B} < X_{\rm B,2}^{\rm s}$, where equilibrium according to the double-tangent construction requires two-phase coexistence, do not reach inflection points there, but rather cross [Fig. 6(b)]. Heuristically, we have terminated these metastable branches near the crossing points. In the plot of $\Delta\mu - \Delta\mu_{\rm coex}$, we have connected the metastable branches by a vertical line located such that the equal area rule is satisfied [Fig. 6(a)]. These vertical lines in Fig. 6(a) do not correspond to any physically realizable states. Rather, as is well-known from other cases of isotropic-nematic transitions,[58] the metastable homogeneous isotropic and nematic branches of $G_{\rm exc}$ (and $\Delta\mu$) would continue beyond this point of the vertical lines, even into the region where no longer any two-phase coexistence occurs: The stability limit of the isotropic phase is inside the region of the homogeneous nematic phase, and *vice versa*.

This behavior may seem surprising at first, but it can be understood by considering that the primary order parameter for the I-N transition is the nematic order parameter $Q_{\alpha\beta}$, unlike standard fluid binary mixtures where the concentration difference $X_{\rm B,1}^{\rm coex} - X_{\rm B,2}^{\rm coex}$

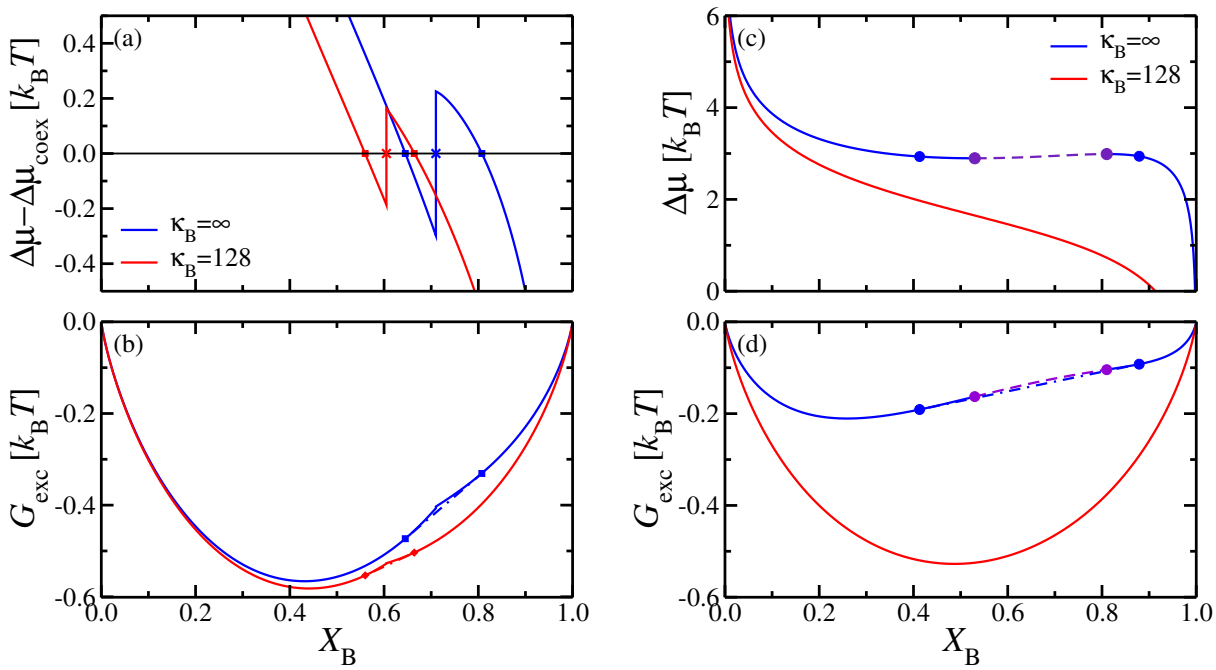

Figure 6: (a) Difference between the chemical potentials of the two components $\Delta\mu = \mu_A - \mu_B$ relative to its value at coexistence $\Delta\mu_{coex}$ *vs.* X_B for $\kappa_B = \infty$ and $\kappa_B = 128$. Symbols indicate the values of X_B in the two phases at coexistence. (b) Gibbs excess free energy relative to the corresponding ideal binary mixture G_{exc}. The dot-dashed lines connecting the symbols indicate the common tangent construction. All DFT results in (a,b) were obtained at pressure $P/P_B^{coex} = 1.3$, *i.e.* $P = 0.14\,k_BT/\sigma^3$ for $\kappa_B = \infty$ and $P = 0.18\,k_BT/\sigma^3$ for $\kappa_B = 128$, respectively. (c) Plot of $\Delta\mu$ *vs.* X_B at $P = 0.5\,k_BT/\sigma^3$. The blue circles indicate X_B in the two phases at coexistence, while the purple circles correspond to the spinodal boundaries. (d) Same as (b) but for $P = 0.5\,k_BT/\sigma^3$.

is the order parameter instead. This fact is readily recognized when we consider the I-N phase transition in the plane of intensive variables P and $\Delta\mu$, as shown in Fig. 4(e). The transition is a first order transition occurring at $P_t(\Delta\mu)$, and metastable isotropic states are expected up to a line $P_{s,1}(\Delta\mu) > P_t(\Delta\mu)$, while metastable nematic states are expected for $P_{s,2}(\Delta\mu) < P < P_t(\Delta\mu)$. One can consider this situation likewise for varying $\Delta\mu$ at fixed P, rather than varying P at fixed $\Delta\mu$. In the (P, X_B) ensemble, the first order line $P_t(\Delta\mu)$ in the $(P, \Delta\mu)$-plane is split into the two-phase coexistence region in between $X_{B,2}^{coex} - X_{B,1}^{coex}$, and from this consideration it is obvious that $X_{B,2}^{coex} - X_{B,1}^{coex}$ is not the primary order parameter as in a standard binary fluid mixture.

It is well-known that spinodals (stability limit of metastable states) have limited physical

significance. The practical stability limit is realized when the free energy barrier against homogeneous nucleation of the stable phase is no longer very large.[59] Thus, we have not attempted to locate the spinodals that DFT would predict. But we note that considerable metastability of both the homogeneous isotropic and nematic phases was observed in the MD simulations. Mixed phase configurations [Fig. 4(c,d)] could only be observed when suitable heterogeneous initial states were used.

The situation is qualitatively different for the case $\kappa_{\rm B} = \infty$ at high pressures $P = 0.5\, k_{\rm B}T/\sigma^3$, where an unmixing transition between two nematic phases occurs. For the two coexisting phases $X_{\rm B,1}^{\rm coex}$ and $X_{\rm B,2}^{\rm coex}$, which are both nematic (though the values of their nematic order parameters may be different), the concentration difference $X_{\rm B,2}^{\rm coex} - X_{\rm B,1}^{\rm coex}$ is the primary order parameter. Indeed the loop of $\Delta\mu$ *vs.* $X_{\rm B}$ has then the familiar van der Waals form [Fig. 6(c)]. For stiff but not strictly rigid chains ($\kappa_{\rm B} = 128$), this phase separation is no longer present, and $\Delta\mu$ *vs.* $X_{\rm B}$ shows a monotonic decrease. In order to understand this qualitatively different behavior of fully rigid and slightly flexible rods, we decompose $G_{\rm exc}$ into its four components, *i.e.*, the translational $G_{\rm exc}^{\rm transl}$, the mixing $G_{\rm exc}^{\rm mix}$, the orientational entropy $G_{\rm exc}^{\rm orient}$, and the excluded volume $G_{\rm exc}^{\rm excl}$ terms. These four contributions are obtained as follows[55,60]

$$G_{\rm exc}^{\rm transl} = \ln(\rho/N) - (1 - X_{\rm B})\ln(\rho_{\rm A}^0/N) - X_{\rm B}\ln(\rho_{\rm B}^0/N), \tag{12}$$

where ρ_i^0 is the (monomer) density of the pure $i^{\rm th}$ component at the given pressure;

$$G_{\rm exc}^{\rm mix} = (1 - X_{\rm B})\ln(1 - X_{\rm B}) + X_{\rm B}\ln(X_{\rm B}), \tag{13}$$

$$G_{\rm exc}^{\rm orient} = (1 - X_{\rm B})(S_{\rm orient,A} - S_{\rm orient,A}^0) + X_{\rm B}(S_{\rm orient,B} - S_{\rm orient,B}^0), \tag{14}$$

where $S_{\rm orient,i}$ ($S_{\rm orient,i}^0$) is the orientational entropy of the $i^{\rm th}$ component in the binary mixture

(pure state); and finally

$$G_{\rm exc}^{\rm excl} = (1 - X_{\rm B})(G_{\rm excl,A} - G_{\rm excl,A}^{0}) + X_{\rm B}(G_{\rm excl,B} - G_{\rm excl,B}^{0}), \tag{15}$$

where $G_{\rm excl,i}$ ($G_{\rm excl,i}^{0}$) is the excluded volume Gibbs free energy of the $i^{\rm th}$ component in the binary mixture (pure state).

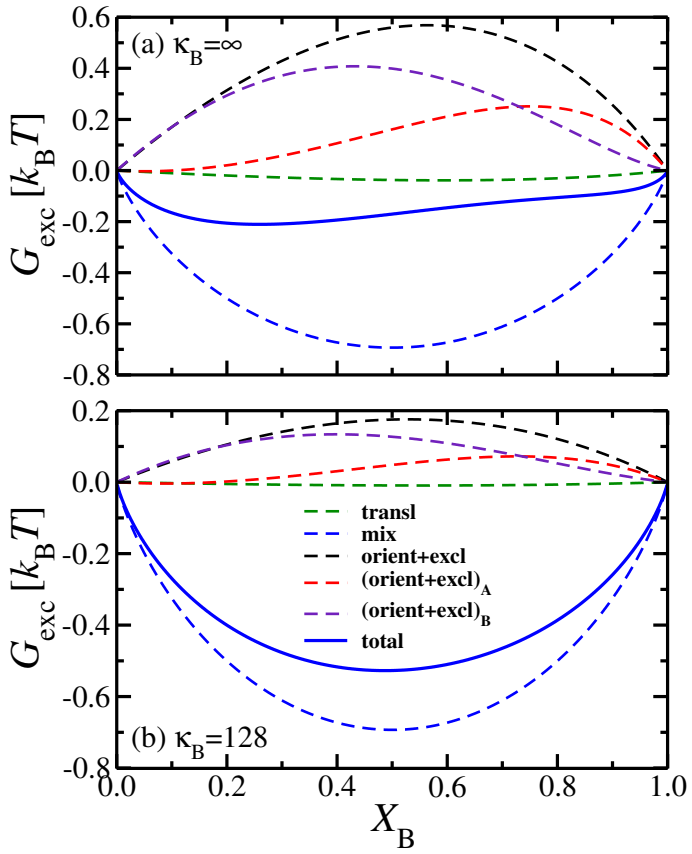

Figure 7: The contributions to the Gibbs excess free energy $G_{\rm exc}$ along the isobar $P = 0.5\,k_{\rm B}T/\sigma^3$ *vs.* $X_{\rm B}$ for (a) $\kappa_{\rm B} = \infty$ and (b) $\kappa_{\rm B} = 128$ ($\kappa_{\rm A} = 24$ fixed in both cases). The energy $G_{\rm exc}$ is decomposed into translational [Eq. (12)], the mixing [Eq. (13)], and the sum of orientational entropy [Eq. (14)] and excluded volume [Eq. (15)] terms, the latter is split into the contributions from the A and B component.

These individual contributions to the Gibbs excess free energy are plotted together with its total value in Fig. 7 as functions of the mole fraction of the stiffer component $X_{\rm B}$ along the isobar $P = 0.5\,k_{\rm B}T/\sigma^3$. Figure 7(a) shows the results for the fully rigid second component $\kappa_{\rm B} = \infty$, while Fig. 7(b) corresponds to the case $\kappa_{\rm B} = 128$. The total $G_{\rm exc}$ for $\kappa_{\rm B} = 128$

is *concave* in the entire range of X_{B}, *i.e.*, the binary mixture is fully miscible for all mole fractions of the stiffer component, in contrast to the fully rigid B chains, where the *convex* portion of G_{exc} indicates N-N phase separation, as already illustrated in Fig. 6(a,b) *via* equal area and common tangent constructions, respectively. The following observations regarding individual contributions to G_{exc} can be made: First, both translational and mixing terms favor mixing, while the orientational entropy and excluded volume terms (which are plotted together as a sum) promote unmixing, which is in agreement with the conclusions reached in the literature.[55,60] A key difference between the case $\kappa_{\mathrm{B}} = \infty$ and $\kappa_{\mathrm{B}} = 128$ is the fact that the sum of orientational and excluded volume terms is significantly larger for the fully rigid second component [black line in Fig. 7(a)] compared to slightly flexible rods [black line in Fig. 7(b)]. Finally, when the latter term is split into the contributions from individual components (*i.e.* the sums of first terms in Eqs. (14) and (15) for the more flexible component and the sums of the corresponding second terms for the stiffer component), one sees that the contribution from the stiffer component largely dominates.

3.3 Nematic Order Parameter

In order to further clarify the reasons for the observed trends, we next consider the order parameters along the same isobar $P = 0.5\, k_{\mathrm{B}}T/\sigma^3$. We define the total order parameter as follows:[55]

$$S = (1 - X_{\mathrm{B}})S_{\mathrm{A}} + X_{\mathrm{B}}S_{\mathrm{B}}, \tag{16}$$

where S_{A} and S_{B} are the order parameters of the two components in the mixture. In addition, we define the excess order parameter relative to an ideal mixture:

$$\Delta S = \Delta S_{\mathrm{A}} + \Delta S_{\mathrm{B}} = (1 - X_{\mathrm{B}})(S_{\mathrm{A}} - S_{\mathrm{A},0}) + X_{\mathrm{B}}(S_{\mathrm{B}} - S_{\mathrm{B},0}), \tag{17}$$

where $S_{\mathrm{A},0}$ and $S_{\mathrm{B},0}$ are the order parameters of the pure components. The total and excess order parameters defined above are plotted in Figs. 8(a-d) as functions of X_{B} along the isobar

$P = 0.5\, k_{\mathrm{B}}T/\sigma^3$. As expected, S_{B} for fully rigid rods is larger compared to slightly flexible ones over the entire X_{B} range. The excess order parameter ΔS is positive in both cases, and is largely dominated by the contribution from the first component, ΔS_{A}, indicating that the stiffer component imposes stronger ordering of the flexible one in the binary mixture relative to the ideal mixture. At the same time, ΔS_{B} is slightly negative for both values of κ_{B}, suggesting that the stiffer component is slightly less ordered in the mixture, most likely due to the fact that the excess density of the mixture (relative to the ideal one) is also slightly negative (not shown). This slight loss of the orientational order of the stiffer component does not have any strong effect on the values of $G_{\mathrm{exc}}^{\mathrm{orient}}$ and $G_{\mathrm{exc}}^{\mathrm{excl}}$ for this component in the case $\kappa_{\mathrm{B}} = 128$ [see Fig. 7(b)], but does have a pronounced effect on these quantities for the fully rigid rods [see Fig. 7(a)]. One possible reason for this different behavior is that the orientational distribution function of rigid rods is much narrower compared to the one of slightly flexible ones (if the two distributions are fit to Gaussian functions, then the decay parameter of the former is up to an order of magnitude larger compared to the latter). As a result, a slight variation in the distribution function upon mixing (as reflected by a small and negative ΔS_{B} in the mixture) can have a strong effect on both orientational entropy and excluded volume free energy of the rigid rods, sufficient to cause the unmixing. This interpretation is somewhat different from the standard explanation of N-N unmixing discussed in the literature.[55] Its driving force is usually attributed to the more flexible component, which is forced to order more strongly in the mixture (as our results for ΔS_{A} confirm), and therefore can gain orientational entropy upon unmixing, which could be sufficient to offset the loss of mixing free energy. At the same time, for our particular model and set of parameters, it appears that the stiffer component plays an important role, because its slight loss of the orientational order in the mixture leads to a substantial increase of its excluded volume excess free energy when it is fully rigid.

Further, note that both $\Delta\mu$ and G_{exc} exhibit a discontinuous jump in the I-N coexistence region [see Fig. 6(a,b)], while both these quantities vary smoothly as a function of X_{B} in

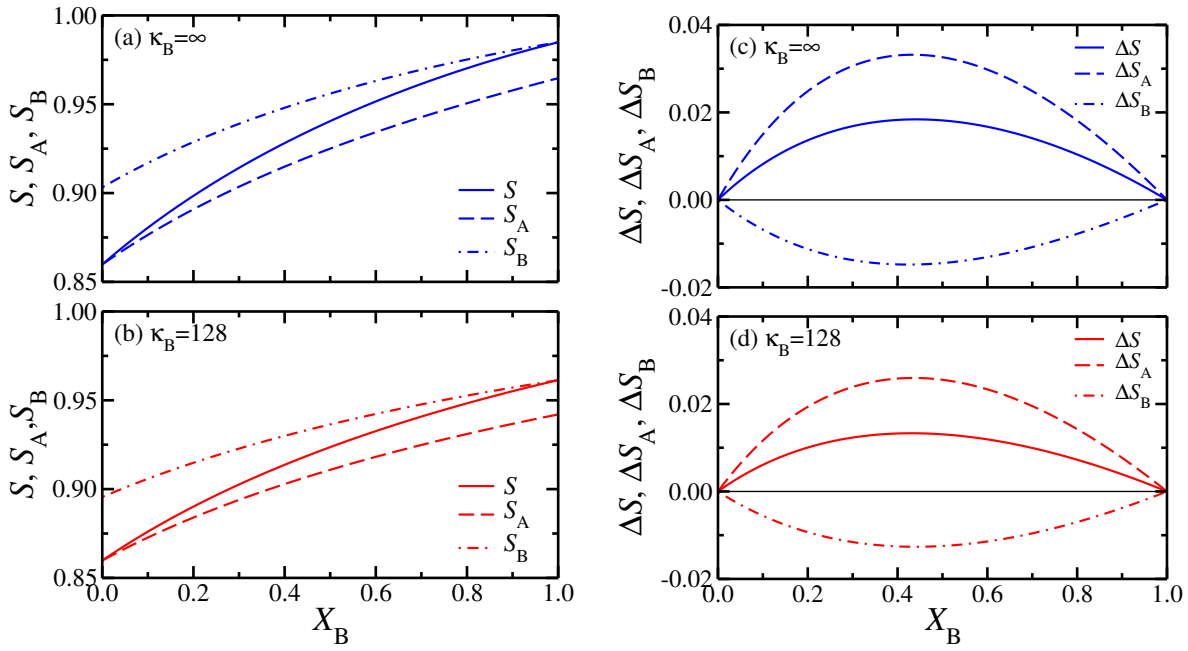

Figure 8: (a,b) Total order parameters S [defined by Eq. (16)] along the isobar $P = 0.5\,k_{\rm B}T/\sigma^3$ *vs.* $X_{\rm B}$ for (a) $\kappa_{\rm B} = \infty$ and (b) $\kappa_{\rm B} = 128$ ($\kappa_{\rm A} = 24$ fixed in both cases). (c,d) Same as (a,b) but for the excess order parameters ΔS [defined by Eq. (17)].

the N-N two-phase region [see Fig. 6(c,d)]. The reason for this difference stems from the fact that the I-N case corresponds to the phase equilibrium between ordered and disordered phases, while both phases are ordered (although to a different extent) in the N-N case. These two types of behavior in a coexistence region have been discussed by Klushin *et al.*[61] in the context of nematic brushes. An interesting aspect of Fig. 8 also is that the crossing of the N-N two-phase coexistence region for $\kappa_{\rm B} = \infty$ and $P = 0.5\,k_{\rm B}T/\sigma^3$ does not lead to any singularities in the variation of S with $X_{\rm B}$.

In view of possible experiments, where a system can be studied at fixed composition varying the monomer density by adding solvent (which also amounts to a change of the osmotic pressure P in the system), we consider in Figs. 9 and 10 the variation of the order parameters $S_{\rm A}$ and $S_{\rm B}$ at fixed $X_{\rm B} = 0.5$ with P (or the total density ρ of monomeric units). In the corresponding pure systems ($X_{\rm B} = 0$ or $X_{\rm B} = 1$), the order parameters jump discontinuously from zero to a non-zero value (near 0.6 in our case) at the pressure $P_{\rm t}$ of the I-N transition, and then they increase smoothly with increasing pressure. For the mixed

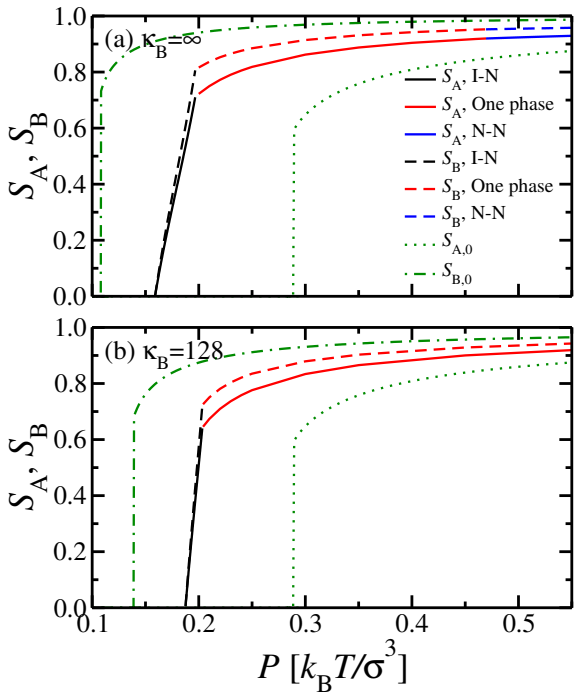

Figure 9: (a,b) Nematic order parameters $S_{\rm A}$ and $S_{\rm B}$ of the A chains (solid) and B chains (dashed) from DFT calculations for (a) $\kappa_{\rm B} = \infty$ and (b) $\kappa_{\rm B} = 128$ *vs.* the overall pressure P of the binary mixture. Nematic order parameters obtained from the lever rule assuming the simulated mole fraction of the stiffer component $X_{\rm B}^{\rm MD} = 0.5$. Black lines: two phase I-N region; red lines: two phase N-N region; blue lines: one phase region.

systems ($X_{\rm B} = 0.5$), however, the first order transition is split in a two phase-coexistence region, and hence one gets a linear increase of $S_{\rm A}$ and $S_{\rm B}$ from zero (at the boundary of the mixed phase) to the values at the boundary of the mixed nematic region. These values are different from their counterparts in the pure systems: $S_{\rm A}$ is larger due to the ordering field caused by the neighboring stiffer B chains, whereas $S_{\rm B}$ is smaller than its pure B phase analog, since part of the neighbors of a B chain are the less stiff A chains.

Comparing the case $\kappa_{\rm A} = 32$, $\kappa_{\rm B} = 128$ to the case $\kappa_{\rm A} = 24$, $\kappa_{\rm B} = 128$ (see Fig. 10) shows that the slope of the straight lines in the two-phase coexistence region are much larger for $\kappa_{\rm A} = 32$, as expected, since this region is much narrower than for $\kappa_{\rm A} = 24$. For chains that differ only slightly in stiffness, the width of the two-phase region would presumably be very hard to resolve. Note that the order parameters shown in Figs. 9 and 10 always refer to the chain orientation as a whole, unlike previous MD work where the bond order parameter $S_{\rm b}$

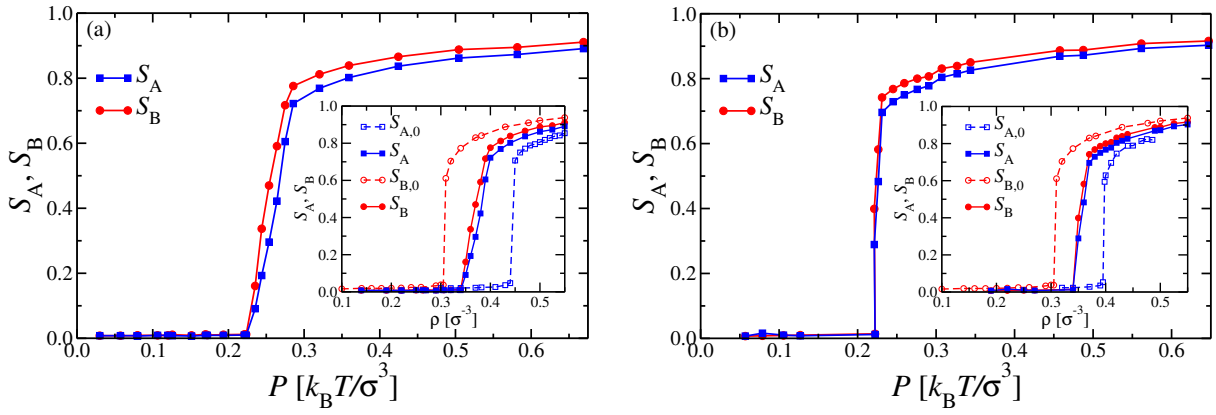

Figure 10: (a) Nematic order parameters S_A, S_B of the A- and B-components *vs.* pressure P with stiffness parameters $\kappa_A = 24$ and $\kappa_B = 128$, respectively, at composition $X_B = 0.5$. The insets show S_A, S_B *vs.* monomer density ρ in the A-B-mixture along with the order parameters $S_{A,0}$, $S_{B,0}$ in the corresponding pure phases. (b) The same as in (a) but for $\kappa_A = 32$, $\kappa_B = 128$ at composition $X_B = 0.5$.

was analyzed for the same model.

When the amount of solvent is varied in an experiment, the monomer density rather than the osmotic pressure becomes the directly accessible control variable. Thus, we have also obtained *via* MD the variation of nematic order parameters *vs.* the total monomer density for the corresponding systems at $X_B = 0.5$ [insets of Fig. 10]. The behavior is qualitatively similar to the case where P is used as a control variable; however, one should note that the variation of S with ρ is not strictly linear in the two-phase coexistence region, because the densities of the two coexisting phases differ [*cf.* Fig 4(c)]. In that case, the phase diagram in the ρ-X_B plane needs to be used to construct the amounts of the coexisting phases at each state point.

3.4 Chain conformations in mixtures

An interesting question concerns the interplay of the conformations of the chains with the phase changes that occur in the system. Figure 11(a) shows profiles of the squared components of the radius of gyration tensor parallel and perpendicular to the nematic director, for the same system ($\kappa_A = 24$ and $\kappa_B = 128$) for which the monomer density profiles have

already been presented in Fig. 4(c). Visual inspection of the simulation snapshots [Fig. 4(d)] and an analysis of the order parameters S_{A} and S_{B} revealed that a nematic domain extends in the considered system from about $x = -5$ to about $x = 95$, while the rest of the system is isotropic. The nematic director here is oriented along the z-axis of the simulation box, due to the choice of initial conditions. The two phases are separated by two interface planes oriented perpendicular to the x-axis, as desired. In the isotropic phase, there is no distinction between parallel and perpendicular components, and the radii for the stiffer chains ($\kappa_{\mathrm{B}} = 128$) are slightly larger than the less stiff ones ($\kappa_{\mathrm{A}} = 24$). In the nematic phase, this difference is quite pronounced for the parallel components but hardly visible for the perpendicular ones. The width of the interface between these oriented chains (in the nematic phase) and the randomly oriented ones (in the isotropic phase) is to a very good approximation the same as for the density profiles [see Fig. 4(c)].

Figure 11(b) discusses the renormalization of the effective persistence length (extracted as usual[25,26,49] from the cosine of the angle between subsequent bond vectors along the chains): The enhancement of the persistence length in the nematic phase characterizes the strength of the average "nematic mean field" that each chain experiences due to the environment. Note that for $\kappa_{\mathrm{A}} = 24$ this effect is larger than for $\kappa_{\mathrm{B}} = 128$; for $N = 16$, $\kappa_{\mathrm{B}} = 128$ implies already such a strong stretching of the chains that the nematic environment can cause only a relatively small further enhancement. Note that there is no DFT counterpart to Fig. 11 due to the coarse-graining involved in the Fynewever-Yethiraj procedure, where each chain is represented by a single effective rod.

3.5 The case of strong stiffness mismatch

While for weak enough stiffness mismatch the generic phase diagram of a lyotropic solution of two semiflexible polymers contains a single phase transition from the (homogeneously mixed) isotropic phase to a (homogeneously mixed) nematic phase, the phase diagram topology changes dramatically for strong stiffness mismatch. For intermediate stiffness mismatch,

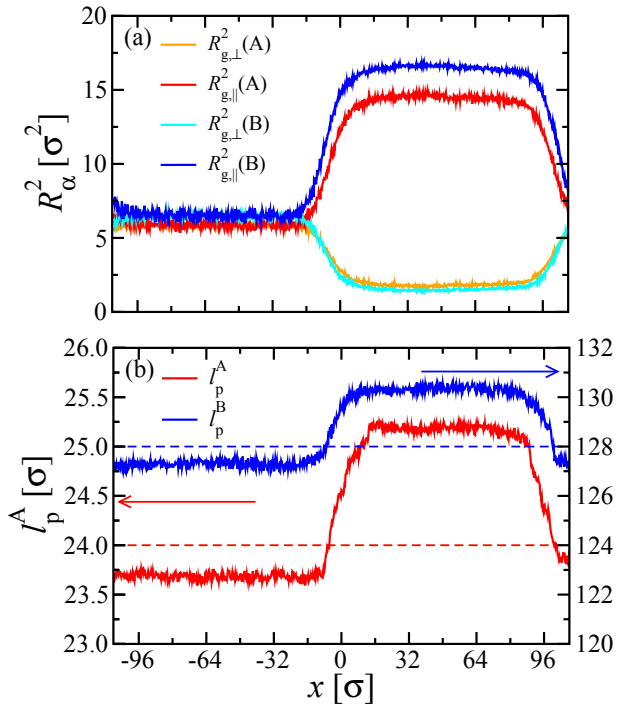

Figure 11: (a) Components of the mean square radius of gyration tensor parallel, $R^2_{g,\parallel}$, and perpendicular, $R^2_{g,\perp}$, to the director field *vs.* the x-coordinate of the center of mass of the chain. Data shown for both A and B chains with $\kappa_A = 24$ and $\kappa_B = 128$, respectively, at $X_B = 0.5$ and total monomer density $\rho = 0.37\,\sigma^{-3}$. (b) Persistence length profiles for the same system as in (a). The scale for the A and B chains are on the left and right side, respectively.

we expect that a N-N miscibility gap may appear at high pressures in the well-ordered nematic phase. This is indeed confirmed in Fig. 12(a), where we plot the phase diagram from DFT for a binary mixture for $\kappa_A = 16$ and $\kappa_B = 128$ in the variables P *vs.* X_B. The closed loop indicates I-N coexistence, and the symbols show X_B in the I and N phases at coexistence at $P = 0.18\,k_BT/\sigma^3$, *i.e.* $P/P_B^{coex} = 1.3$. Dot-dashed lines show N-N coexistence; the corresponding critical point is indicated by a black circle at $X_B^c = 0.605$ and $P_c = 0.9547\,k_BT/\sigma^3$.

It is instructive to compare this phase diagram to the case of a fully rigid second component, which is shown in Fig. 12(b). One sees that the N-N coexistence region moves down to lower pressures and merges with the I-N coexistence region, resulting in a triphase isotropic-nematic-nematic (I-N-N) equilibrium at the pressure $P_t = 0.325\,k_BT/\sigma^3$ corresponding to

the triple point, which is indicated by three black triangles. The coexisting mole fractions of the stiffer component at $P/P_{\rm B}^{\rm coex} = 1.3$ are quite similar in the two cases (as was already seen in Fig. 2), but the overall morphologies of the two phase diagrams are quite different. In this sense, the results shown in Fig. 2, which focus on a single isobar, are by no means representative of the overall phase behavior (this comment pertains to the simulation data as well).

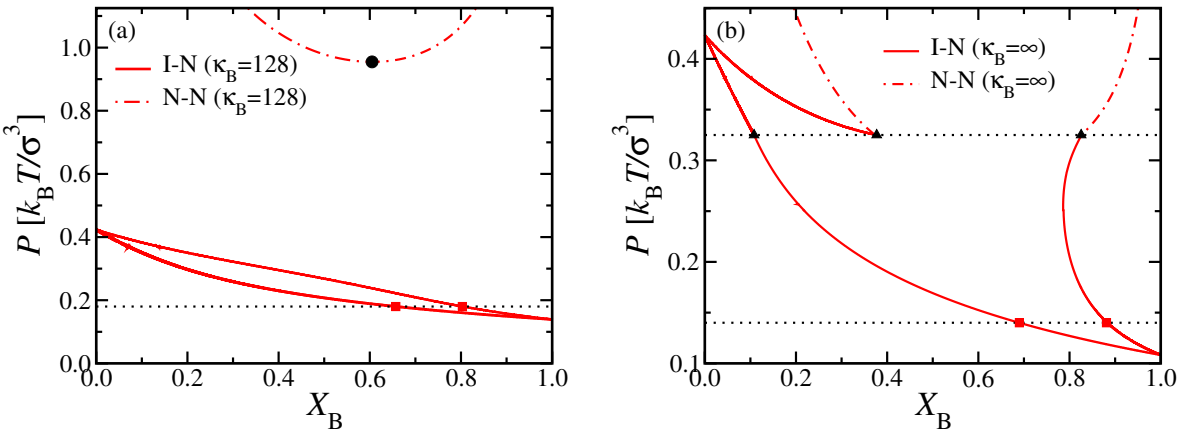

Figure 12: (a) Phase diagram from DFT for $\kappa_{\rm A} = 16$ and $\kappa_{\rm B} = 128$ in the variables P *vs.* $X_{\rm B}$. The closed loop indicates I-N coexistence, and the symbols show $X_{\rm B}$ in the I and N phases at coexistence at $P = 0.18\,k_{\rm B}T/\sigma^3$, *i.e.*, $P/P_{\rm B}^{\rm coex} = 1.3$. Dot-dashed lines show N-N coexistence. The corresponding critical point is indicated by a black circle at $X_{\rm B}^{\rm c} = 0.605$ and $P_{\rm c} = 0.9547\,k_{\rm B}T/\sigma^3$. (b) Same as (a) but for $\kappa_{\rm A} = 16$ and $\kappa_{\rm B} = \infty$. The solid lines indicate I-N coexistence, and the symbols show $X_{\rm B}$ in the I and N phases at coexistence at $P = 0.14\,k_{\rm B}T/\sigma^3$, *i.e.*, $P/P_{\rm B}^{\rm coex} = 1.3$. Dot-dashed lines show N-N coexistence; the triple point is indicated by three black triangles at $P_{\rm t} = 0.325\,k_{\rm B}T/\sigma^3$.

Proceeding to even larger stiffness disparity, we set $\kappa_{\rm A} = 8$ and present the corresponding DFT phase diagrams for $\kappa_{\rm B} = 128$ and $\kappa_{\rm B} = \infty$ in Figs. 13(a) and 13(b), respectively. In this case, the triphase I-N-N equilibrium is observed already for $\kappa_{\rm B} = 128$, with the triple point pressure $P_{\rm t} = 0.934\,k_{\rm B}T/\sigma^3$. In addition, reentrant behavior is observed for $X_{\rm B} > 0.9$ in this case. By contrast, in the case of the rigid second component, DFT predicts a complete I-N phase separation into two pure components for $0.7\,k_{\rm B}T/\sigma^3 \lesssim P < P_{\rm A}^{\rm coex} = 0.998\,k_{\rm B}T/\sigma^3$. Above $P_{\rm A}^{\rm coex}$, one expects to see two immiscible nematic phases of pure components A and B. Once again, the coexisting mole fractions at $P/P_{\rm B}^{\rm coex} = 1.3$ are quite similar in the two

cases (as was already seen in Fig. 2), but the overall morphologies of the two phase diagrams are quite different.

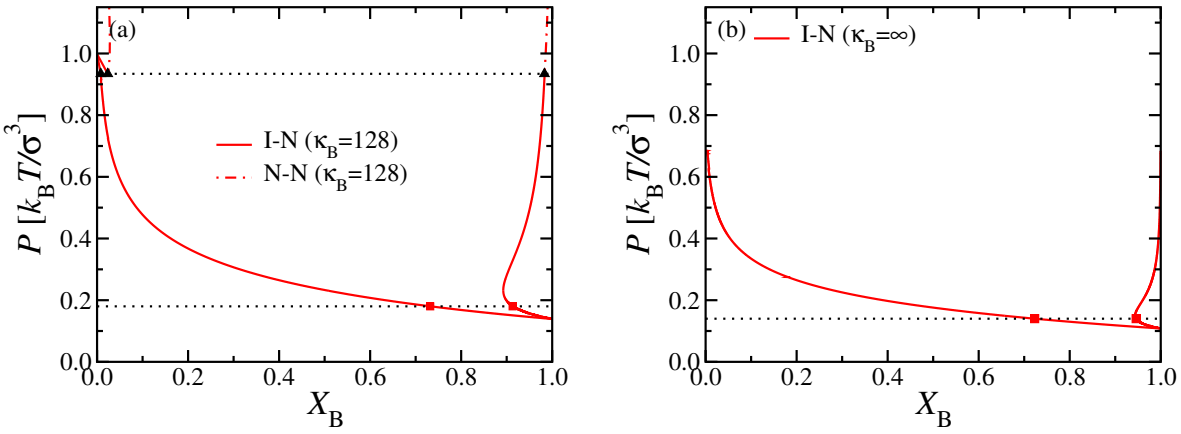

Figure 13: (a) Phase diagram from DFT for $\kappa_{\rm A} = 8$ and $\kappa_{\rm B} = 128$ in the variables P *vs.* $X_{\rm B}$. The solid lines indicate I-N coexistence, and the symbols show $X_{\rm B}$ in the I and N phases at coexistence at $P = 0.18\, k_{\rm B}T/\sigma^3$, *i.e.*, $P/P_{\rm B}^{\rm coex} = 1.3$. Dot-dashed lines show N-N coexistence; the triple point is indicated by three black triangles, $P_{\rm t} = 0.934\, k_{\rm B}T/\sigma^3$. (b) Same as (a) but for $\kappa_{\rm A} = 8$ and $\kappa_{\rm B} = \infty$. The solid lines indicate I-N coexistence, and the symbols show $X_{\rm B}$ in the I and N phases at coexistence at $P = 0.14\, k_{\rm B}T/\sigma^3$, *i.e.*, $P/P_{\rm B}^{\rm coex} = 1.3$.

So far, we have focused exclusively on the case $N_{\rm A} = N_{\rm B} = 16$, where the I-N coexistence pressure for the more flexible component becomes rather high for small values of $\kappa_{\rm A}$ [as seen, *e.g.*, in Fig. 13(a)], and therefore the predicted DFT behavior could be potentially preempted by the appearance of smectic phase(s). Hence, it would be of interest to consider somewhat longer chains. Indeed, preliminary DFT work shows that then the phase diagram topology of Fig. 13(b) is found also for the case $\kappa_{\rm A} = 24$, $\kappa_{\rm B} = \infty$ if $N_{\rm A} = N_{\rm B} = 32$.

While our theoretical phase diagrams were presented in the variables P *vs.* $X_{\rm B}$, in the experimental literature it is common to present the data in the form of a triangular ternary phase diagram with the three corresponding mole fractions, *i.e.*, the two components of the binary mixture and the solvent. In our approach the solvent is treated implicitly, and there is no incompressibilty constraint (such as commonly imposed in lattice-based self consistent field theory calculations). As a result, the total packing fraction is somewhat ill-defined. In order to construct a triangular phase diagram, we arbitrarily set the total density (monomers plus solvent) to $0.8\,\sigma^{-3}$ (our implicit solvent model reaches the crystalline phase at about

this density). The resulting triangular phase diagram is presented in Fig. 14 for a binary mixture of 16-mers with $\kappa_A = 24$ and $\kappa_B = 128$. In this representation, the right end-point of the base corresponds to $X_B = 1$, the left end-point of the base corresponds to $X_A = 1$, while the upper corner corresponds to a pure solvent $X_S = 1$. The circles connected by dashed tie-lines mark the coexisting systems. Remember that the perfect miscibility in the nematic phase in Fig. 14 is a consequence of our model assumption that the only difference between A and B chains is stiffness disparity. Near the upper corner, the state of the system is a mixed isotropic phase and in the lower part of the triangle it is a homogeneously mixed nematic phase. Note that further phases such as smectics and crystalline solids[50] are expected near the baseline in Fig. 14, but are not included in the phase diagrams here.

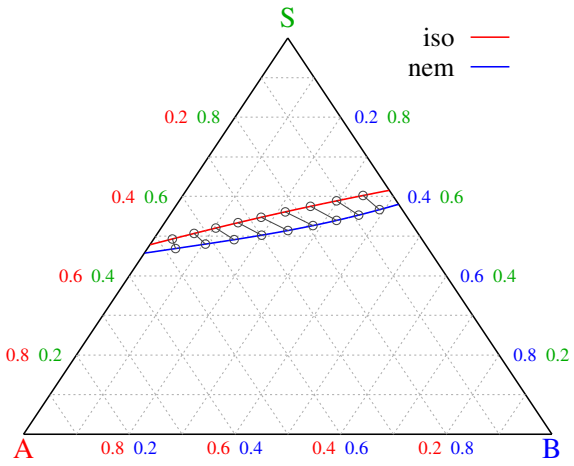

Figure 14: Triangular ternary phase diagram for a binary mixture of 16-mers with $\kappa_A = 24$ and $\kappa_B = 128$. At the right end-point of the base $X_B = 1$, at the left end-point of the base $X_A = 1$, while the upper corner corresponds to pure solvent $X_S = 1$. The circles connected by dashed tie-lines mark the coexisting systems.

4 Discussion and Conclusions

While blending of different flexible polymers is standard practice for producing polymeric materials with improved application properties, much less is known about how mixing of different kinds of semiflexible or stiff polymers affects the properties of the resulting materials, which might have applications as strong fibers or as parts in liquid-crystalline devices. As a

first step of dealing with such questions, we have considered lyotropic solutions where two polymers of comparable contour length but different stiffness exist in a common solvent. To focus on the effect of stiffness disparity between the two kinds of chains (A and B), we have assumed ideal good solvents of precisely the same quality, so that no enthalpic driving force towards separation into A-rich or B-rich phases exists. In many real systems, such an enthalpic driving force may also be present, but the theoretical model used here allows us to isolate the entropic effects due to the interplay of configurational entropy and bending stiffness. Additional enthalpic effects could then be added later, in the spirit of standard Flory-Huggins type treatment and their extensions for blends formed from flexible polymers.

The considered constituents (polymer A + solvent S and polymer B + solvent S, respectively) exhibit a transition from an isotropic phase (at large enough solvent concentrations) to a nematic phase (at smaller solvent concentration). We focus here on the question of how the character of these isotropic and nematic phases changes when we consider mixtures rather than the corresponding pure phases. Such problems can be conveniently addressed by Density Functional Theory (DFT) for a wide variety of parameters, such as the chain lengths N_{A}, N_{B}, polymer stiffnesses κ_{A}, κ_{B}, and densities ρ_{A}, ρ_{B} of the corresponding monomeric units in the solution *etc.* Hence, we have developed an extension of DFT, which was previously applied successfully to solutions of a single kind of polymer. This extension is not at all trivial, since it requires the excluded volume between different types of chains as a function of the angle between their molecular axes. This task was achieved by extensive Monte Carlo (MC) averaging of a large number of samples of corresponding chain conformations (see Fig. 1). Although the differences between the results for pairs of equal types of chains and unequal ones are rather small, Fig. 1, they have nevertheless pronounced effects on the resulting phase behavior. Since DFT involves several approximations, which cannot be controlled *a priori*, we have tested the accuracy of DFT by extensive comparison to both previous MC results available in the literature[33] (see Fig. 2) and new Molecular Dynamics (MD) results obtained by us. We focused on the case of rather short chains consisting of

$N_A = N_B = 16$ effective monomeric units, and use persistence lengths either on the order of the chain length, or considerably larger, up to the rigid rod limit. Surprisingly, we found that even if the persistence length exceeds the chain contour length by a factor of 8, the results still differ significantly from the rigid rod limit [Figs. 3(a), 4(a)]. For rigid rods, even a separation into two distinct nematic phases is predicted at high enough osmotic pressure (or density of monomeric units). For chains with some flexibility, this latter transition is preempted by other (smectic or crystalline) phases occurring at high enough density, which are not studied here. But nematic-nematic coexistence can be found in suitable cases for significantly longer chains, where also the isotropic-nematic transition is found at lower osmotic pressure.

While the isotropic-nematic transition in pure polymer-solvent systems is characterized by an extremely narrow two-phase coexistence region (the density of monomer units ρ_i, ρ_n in units of the corresponding melt density differ only by 1 % or so), much wider isotropic-nematic coexistence regions occur in the mixed systems (Figs. 9 and 10). In the space of variables ρ and mole fraction X_B, the orientation of the tie lines is highly nontrivial, and with increasing stiffness disparity the width of the two-phase coexistence regions also widens. This effect is a precursor of the change of the phase diagram that occurs for very strong stiffness mismatch, where a triple point appears separating the isotropic phase, and B-rich and A-rich nematic phases (Figs. 12 and 13). All these findings can be explained in detail by an analysis of the Gibbs excess free energy and the various terms contributing to it (translational part, free energy of mixing, orientational contributions). Such a detailed analysis of the microscopic origins of different features of phase behavior is only possible with the DFT framework (Figs. 6 and 7). MD, however, can supplement innformation on chain conformations in the different phases. In fact, the mismatch of the conformation of a minority chain to the influence of the environment in which it resides is crucial for the driving forces for the observed phase separations.

Acknowledgments

We thank the German Research Foundation (DFG) for support under project numbers BI 314/24-2, NI 1487/4-2, NI 1487/2-1, and NI 1487/2-2. S.A.E. thanks the Alexander von Humboldt Foundation for support. The authors gratefully acknowledge the computing time granted on the supercomputer Mogon (hpc.uni-mainz.de). A.M. thanks the COST action No. CA17139, supported by COST (European Cooperation in Science and Technology) and its Bulgarian partner FNI/MON under KOST-11.

References

(1) Flory, P. J. *Principles of Polymer Chemistry*; Cornell University Press, Ithaca, New York, 1953.

(2) Strobl, G. R., Ed. *The Physics of Polymers: Concepts for Understanding Their Structures and Behavior*, 3rd ed.; Springer, Berlin, 2007.

(3) Paul, D. R., Bucknall, C. B., Eds. *Polymer Blends, Vol 1 and 2*; Wiley, New York, 2000.

(4) Konigsveld, R.; Stockmayer, W. H.; Nies, E. *Polymer Phase Diagrams*; Oxford University Press, Oxford, 2001.

(5) Rubinstein, M.; Colby, R. H. *Polymer Physics*; Oxford University Press, Oxford, 2003.

(6) Binder, K. Phase Transitions in Polymer Blends and Block-Copolymer Melts: Some Recent Developments. *Adv. Polym. Sci.* **1994**, *112*, 181–299.

(7) Enders, S., Wolf, B. A., Eds. *Polymer Thermodynamics: Liquid Polymer-Containing Mixtures*, 1st ed.; Springer, Heidelberg, 2011.

(8) Ciferri, A., Krigbaum, W. R., Meyer, R. B., Eds. *Polymer Liquid Crystals*; Academic Press, New York, 1982.

(9) Ciferri, A., Ed. *Liquid Crystallinity in Polymers: Principles and Fundamental Properties*, 1st ed.; VCH Publishers, New York, 1991.

(10) Donald, A. M.; Windle, A. H.; Hanna, S. *Liquid Crystalline Polymers*; Cambridge University Press, Cambridge, 2006.

(11) Claessens, M. M. A. E.; Tharmann, R.; Kroy, K.; Bausch, A. R. Microstructure and Viscoelasticity of Confined Semiflexible Polymer Networks. *Nat. Phys.* **2006**, *2*, 186.

(12) Kasza, K. E.; Rowal, A. C.; Liu, J.; Angelini, T. E.; Brangwynne, C. P.; Koenderink, G. H.; Weitz, D. A. The Cell as a Material. *Curr. Opin. Cell Biol.* **2007**, *19*, 101.

(13) Fletcher, D. A.; Mullins, R. D. Cell Mechanics and the Cytoskeleton. *Curr. Opin. Cell Biol.* **2010**, *463*, 485.

(14) Purdy, K. R.; Varga, S.; Galindo, A.; Jackson, G.; Fraden, S. Nematic Phase Transitions in Mixtures of Thin and Thick Colloidal Rods. *Phys. Rev. Lett.* **2005**, *94*, 057801.

(15) Dennison, M.; Dijkstra, M.; van Roij, R. The Effects of Shape and Flexibility on Bio-Engineered fd-Virus Suspensions. *J. Chem. Phys.* **2011**, *135*, 144106.

(16) Dennison, M.; Dijkstra, M.; van Roij, R. Phase Diagram and Effective Shape of Semiflexible Colloidal Rods and Biopolymers. *Phys. Rev. Lett.* **2011**, *106*, 208302.

(17) Semenov, A. N.; Subbotin, A. V. Phase Equilibria in Mixtures of Rigid Chain Polymers. *Polym. Sci. U.S.S.R.* **1989**, *31*, 2266–2273.

(18) Grosberg, A. Y.; Khokhlov, A. R. Statistical Theory of Polymeric Lyotropic Liquid Crystals. *Adv. Polym. Sci.* **1981**, *41*, 53–97.

(19) Sato, T.; Teramoto, A. Concentrated Solutions of Liquid-Crystalline Polymers. *Adv. Polym. Sci.* **1996**, *126*, 85–161.

(20) Binder, K.; Egorov, S. A.; Milchev, A.; Nikoubashman, A. Understanding the Properties of Liquid-Crystalline Polymers by Computational Modeling. *J. Phys. Mater.* **2020**, *3*, 032008.

(21) Khokhlov, A. R.; Semenov, A. N. Liquid-Crystalline Ordering in the Solution of Long Persistent Chains. *Physica A* **1981**, *108*, 546–556.

(22) Khokhlov, A. R.; Semenov, A. R. Liquid-Crystalline Ordering in the Solution of Partially Flexible Macromolecules. *Physica A* **1982**, *112*, 605–614.

(23) Odijk, T. Theory of Lyotropic Polymer Liquid Crystals. *Macromolecules* **1986**, *19*, 2313–2329.

(24) Chen, Z. Y. Nematic Ordering in Semiflexible Polymer Chains. *Macromolecules* **1993**, *26*, 3419–3426.

(25) Egorov, S. A.; Milchev, A.; Binder, K. Anomalous Fluctuations of Nematic Order in Solutions of Semiflexible Polymers. *Phys. Rev. Lett.* **2016**, *116*, 187801.

(26) Egorov, S. A.; Milchev, A.; Virnau, P.; Binder, K. A New Insight into the Isotropic-Nematic Phase Transition in Lyotropic Solutions of Semiflexible Polymers: Density-Functional Theory Tested by Molecular Dynamics. *Soft Matter* **2016**, *12*, 4944–4959.

(27) Scott, R. L. The Thermodynamics of High Polymer Solutions. V. Phase Equilibria in the Ternary System: Polymer 1-Polymer 2-Solvent. *J. Chem. Phys.* **1949**, *17*, 279.

(28) Dobry, A.; Boyer-Kawenoki, F. Phase Separation in Polymer Solution. *J. Polym. Sci.* **1947**, *2*, 90–100.

(29) Dutta, D.; Fruitwala, H.; Kohli, A.; Weiss, R. A. Polymer Blends Containing Liquid Crystals: A Review. *Polym. Eng. Sci.* **1990**, *30*, 1005–1018.

(30) Holyst, R.; Schick, M. Mixtures of Rigid and fFexible Nematogenic Polymers. *J. Chem. Phys.* **1991**, *96*, 721.

(31) Liu, A. J.; Fredrickson, G. H. Free Energy Functionals for Semi-Flexible Polymer Solutions and Blends. *Macromolecules* **1993**, *26*, 2817–2824.

(32) Liu, A. J.; Fredrickson, G. H. Phase Separation Kinetics of Rod/Coil Mixtures. *Macromolecules* **1996**, *29*, 8000–8009.

(33) Escobedo, F. A.; de Pablo, J. J. Monte Carlo Simulation of Athermal Mesogenic Chains: Pure Systems, Mixtures, and Constrained Environments. *J. Chem. Phys.* **1997**, *106*, 9858.

(34) Lekkerkerker, H. N. W.; Tuinier, R. *Colloids and the Depletion Interaction*; Springer, Dordrecht, 2011.

(35) Oyarzun, B.; van Westen, T.; Vogt, T. J. H. Isotropic-Nematic Phase Equilibria of Hard-Sphere Chain Fluids-Pure Components and Binary Mixtures. *J. Chem. Phys.* **2015**, *142*, 064903.

(36) Shundyak, K.; van Roij, R. Free Planar Isotropic-Nematic Interfaces in Binary Hard-Rod Fluids. *Phys. Rev. E* **2003**, *68*, 061703.

(37) Evans, R. Nature of the Liquid-Vapor Interface and Other Topics in the Statistical-Mechanics of Nonuniform, Classical Fluids. *Adv. Phys.* **1979**, *28*, 143–200.

(38) Fredrickson, G. H.; Liu, A. J.; Bates, F. S. Entropic Corrections to the Flory-Huggins Theory of Polymer Blends - Architectural and Conformational Effects. *Macromolecules* **1994**, *27*, 2503–2511.

(39) Kozuch, D. J.; Zhang, W.; Milner, S. T. Predicting the Flory-Huggins χ Parameter for Polymers with Stiffness Mismatch from Molecular Dynamics Simulations. *Polymers* **2016**, *8*, 241.

(40) Milchev, A.; Egorov, S. A.; Midya, J.; Binder, K.; Nikoubashman, A. Entropic Unmixing in Nematic Blends of Semiflexible Polymers. *ACS Macro Lett.* **2020**, *9*, 1779–1784.

(41) Weeks, J. D.; Chandler, D.; Andersen, H. C. Role of Repulsive Forces in Determining the Equilibrium Structure of Simple Liquids. *J. Chem. Phys.* **1971**, *54*, 5237.

(42) Grest, G. S.; Kremer, K. Molecular Dynamics Simulation in the Presence of a Heat Bath. *Phys. Rev. A* **1986**, *33*, 3628(R).

(43) Martyna, G. J.; Tobias, D. J.; Klein, M. L. Constant Pressure Molecular Dynamics Algorithms. *J. Chem. Phys.* **1994**, *101*, 4177–4183.

(44) Martyna, G. J.; Tuckerman, M. E.; Tobias, D. J.; Klein, M. L. Explicit Reversible Integrators for Extended Systems Dynamics. *Mol. Phys.* **1996**, *87*, 1117–1157.

(45) Anderson, J. A.; Glaser, J.; Glotzer, S. C. HOOMD-blue: A Python Package for High-Performance Molecular Dynamics and Hard Particle Monte Carlo Simulations. *Comput. Mater. Sci.* **2020**, *173*, 109363.

(46) Onsager, L. The Effects of Shape on the Interaction of Colloidal Particles. *Ann. N. Y. Acad. Sci.* **1949**, *51*, 627–659.

(47) Fynewever, H.; Yethiraj, A. Phase Behaviour of Semiflexible Tangent Hard Sphere Chains. *J. Chem. Phys.* **1998**, *108*, 1636–1644.

(48) Huang, A.; Bhattacharya, A.; Binder, K. Conformations, Transverse Fluctuations, and Crossover Dynamics of a Semi-Flexible Chain in Two Dimensions. *J. Chem. Phys.* **2014**, *140*, 214902.

(49) Milchev, A.; Egorov, S. A.; Binder, K.; Nikoubashman, A. Nematic Order in Solutions of Semiflexible Polymers: Hairpins, Elastic Constants, and the Nematic-Smectic Transition. *J. Chem. Phys.* **2018**, *149*, 174909.

(50) Milchev, A.; Nikoubashman, A.; Binder, K. The Smectic Phase in Semiflexible Polymer Materials: A Large Scale Molecular Dynamics Study. *Comput. Mat. Sci.* **2019**, *166*, 230–239.

(51) Tortora, M. M. C.; Doye, J. P. K. Incorporating Particle Flexibility in a Density Functional Description of Nematics and Cholesterics. *Mol. Phys.* **2018**, *116*, 2773–2791.

(52) Weinhold, J. D.; Kumar, S. K.; Singh, C.; Schweizer, K. S. Athermal Stiffness Blends - A Comparison of Monte-Carlo Simulations and Integral-Equation Theory. *J. Chem. Phys.* **1995**, *103*, 9460–9474.

(53) Lekkerkerker, H. N. W.; Stroobants, A. Phase-Behavior of Rod-Like Colloid + Flexible Polymer Mixtures. *Nuovo Cimento* **1994**, *16D*, 949–962.

(54) Matsuyama, A.; Kato, T. Phase Diagrams of Polymer Dispersed Liquid Crystals. *J. Chem. Phys.* **1998**, *108*, 2067–2072.

(55) van Westen, T.; Vlugt, T. J. H.; Gross, J. The Isotropic-Nematic and Nematic-Nematic Phase Transition of Binary Mixtures of Tangent Hard-Sphere Chain Fluids: An Analytical Equation of State. *J. Chem. Phys.* **2014**, *140*, 034504.

(56) Gauger, A.; Pakula, T. Phase-Equilibrium in Mixtures of Flexible and Stiff Polymers Studied by Monte Carlo Simulation. *J. Chem. Phys.* **1993**, *98*, 3548–3553.

(57) Ramirez-Hernandez, A.; Hur, S. M.; Armas-Perez, J. C.; Olvera de la Cruz, M.; de Pablo, J. J. Demixing by a Nematic Mean Field: Coarse-Grained Simulations of Liquid Crystalline Polymers. *Polymers* **2017**, *9*, 88.

(58) Spakowitz, A. J.; Wang, Z.-G. Semiflexible Polymer Solutions. I. Phase Behavior and Single-Chain Statistics. *J. Chem. Phys.* **2003**, *119*, 13113.

(59) Binder, K. Theory of First-Order Phase Transitions. *Rep. Prog. Phys.* **1987**, *50*, 783.

(60) Wensink, H. H.; ; Vroege, G. J.; Lekkerkerker, H. N. W. Isotropic-Nematic Density Inversion in a Binary Mixture of Thin and Thick Hard Platelets. *J. Phys. Chem. B* **2001**, *105*, 10610–10618.

(61) Klushin, L. I.; Birshtein, T. M.; Mercurieva, A. A. Microphase Segregation in Bridging Polymeric Brushes: Regular and Singular Phase Diagrams. *Macromol. Theory Simul.* **1998**, *7*, 483–495.